Performance Testing and Internal Probe Measurements of a High Specific Impulse Hall Thruster

by

Noah Zachary Warner

S.B., Aeronautics and Astronautics
Massachusetts Institute of Technology, 2001

Submitted to the Department of Aeronautics and Astronautics
in partial fulfillment of the requirements for the degree of

Master of Science in Aeronautics and Astronautics

at the

MASSACHUSETTS INSTITUTE OF TECHNOLOGY

September 2003

Signature of Author . . . . . .
Department of Aeronautics and Astronautics
August 5, 2003

Certified by . . . . . .
Manuel Martinez-Sanchez
Professor of Aeronautics and Astronautics
Thesis Supervisor

Accepted by . . . . . .
Edward M. Greitzer
H.N. Slater Professor of Aeronautics and Astronautics
Chair, Committee on Graduate Students

Performance Testing and Internal Probe Measurements of a High Specific Impulse Hall Thruster

by

Noah Zachary Warner

Submitted to the Department of Aeronautics and Astronautics
on August 5, 2003 in partial fulfillment of the
requirements for the degree of
Master of Science in Aeronautics and Astronautics

ABSTRACT

The BHT-1000 high specific impulse Hall thruster was used for performance testing and internal plasma measurements to support the ongoing development of computational models. The thruster was performance tested in both single and two stage anode configurations. In the single stage configuration, the specific impulse exceeded 3000s at a discharge voltage of 1000V while maintaining a thrust efficiency of 50 percent. Two stage operation produced higher thrust, specific impulse and thrust efficiency than the single stage configuration at most discharge voltages. The thruster thermal warmup was characterized using a thermocouple embedded in the outer exit ring, and the magnetic field topology was investigated using a Gaussmeter. The single stage thruster configuration was outfitted with a series of axially distributed Langmuir probes to determine plasma properties inside the discharge channel. Probe data were taken at discharge voltages between 300-900V. Axial profiles of electron temperature, electron density, and plasma potential were measured and compared to results of a previously developed two dimensional particle-in-cell simulation of the BHT-1000 thruster. The experimental data matched the simulation results well, particularly in profiles of electron temperature and plasma potential at low discharge voltages. The peak electron temperature was shown to depend on discharge voltage through a power law relationship in both the experimental and simulated data. The greatest discrepancies between experimental data and simulation results were found to be in comparisons of electron density, where it appears that the simulation may be "smearing" the plasma over too wide of an axial region. Hypotheses for this behavior were discussed along with recommendations for future work.

Thesis Supervisor: Manuel Martinez-Sanchez
Title: Professor of Aeronautics and Astronautics

ACKNOWLEDGMENTS

There are many people I must thank for their support in this phase of my life and career. First and foremost, I would like to thank my advisor, Professor Manuel Martinez-Sanchez, for both his enthusiasm and limitless patience. His zeal for scientific research is contagious. Professor Martinez-Sanchez's abilities are unmatched in my experience and that, combined with his jovial nature, make him a wonderful mentor.

I would also like to thank my sources of funding. The Department of Defense has generously supported me personally through a graduate fellowship under the National Defense Science and Engineering Graduate Fellowship Program. The NASA Glenn Research Center provided funding for the High Specific Impulse Hall Thruster Research Program at MIT and Busek, without which this project would not have been possible.

The staff at Busek were incredibly helpful in the completion of this research. I would like to particularly thank James Szabo for his work on this project. I would also like to express my gratitude to Andrew, Bogdan, Bruce, Chris, Charles F., Charles G., Doug, Emile, George K., George M., Henry, Jurg, Kurt, Larry, Marie, Melissa, Mike, Nate, Paul, Rachel, Seth and Vlad. My experience working at Busek was incredibly fun thanks to everyone there, and the research environment there is top notch.

Of course, many friends have helped me along my way. Within the Space Propulsion Laboratory, I would like to thank Yassir, Shannon, Mark, Paulo, Jorge, Kay, Murat and Luis for making the SPL a wonderful lab to call home. I would particularly like to thank Shannon and Yassir for their camaraderie and support during the last winter's months of hard study. Their diligence and humor kept me going through many long days.

Outside the lab, I would like to thank my dear East Coast friends: Adam, Brau, Carlos, Dan, Jen, Kevin, Ollie (actually a West Coast transplant), and Tim have helped me unwind when necessary and also when not necessary (but just for fun). My (originally) West Coast friends have continued their never ending support and I must thank my compadres Alex, Erik, John, Lane and Valdis.

I would not have made it this far in life without the infinite love of my family. My father, Stuart, has been a supportive presence inside my heart since the day I was born. My mother and stepfather, Pamela and Raymond, continue to send their love and encouragement everyday through phone calls, care packages and visits. The confidence and love of my sister and brother, Jessica and Scott, have always helped me believe in myself. They are the best gifts life handed me from the beginning. My uncles, Steve and Richard, have provided wise words and loving encouragement to not only drive me further, but also to help me remain connected to my family's past and to my father.

Finally, I want to thank my companion, Anjli. Her unwavering confidence in my abilities combined with her soothing words have navigated me through troubled waters countless times. She helps bring my seemingly insurmountable obstacles into focus to show them as simple bumps in the road. Anjli has brought nothing but happiness to my life, and I want to thank her for being my best friend.

TABLE OF CONTENTS

LIST OF FIGURES

LIST OF TABLES

NOMENCLATURE

A_e	effective probe area [m^2]
A_p	probe surface area [m^2]
B	magnetic field magnitude [T]
c	exhaust velocity [m/s]
$\bar{c}$	mean thermal speed [m/s]
E_{beam}	exhaust flow kinetic power [W]
e	electron charge [C]
g	gravitational acceleration [m/s^2]
I_d	discharge current [A]
I_e	electron current [A]
I_i	ion current [A]
I_{inner}	current through inner magnet coil [A]
I_{outer}	current through outer magnet coils [A]
I_{sp}	specific impulse [s]
k	Boltzmann constant [J/K]
m_e	electron mass [kg]
m_i	ion mass [kg]
$\dot{m}_a$	anode propellant flow rate [kg/s]
$\dot{m}_c$	cathode propellant flow rate [kg/s]
n_e	electron number density [$1/m^3$]
n_i	ion number density [$1/m^3$]
P_d	discharge power [W]
q_i	ion charge [C]
R_{Larmor}	Larmor radius [m]
R_{probe}	probe radius [m]
T	thrust [N]
T_e	electron temperature [eV, J, K]
v_e	electron velocity [m/s]
V_f	floating potential [V]
V_p	plasma potential [V]
V_s	sheath potential [V]
v_B	Bohm velocity [m/s]
α	energy accommodation coefficient
γ	ratio of specific heats
ε_o	permittivity of free space [F/m]
η	thrust efficiency
$\theta_{1/2}$	plume divergence half angle [rad]
λ_d	Debye length [m]
Φ_d	discharge potential [V]

Chapter 1

INTRODUCTION

1.1 Space Propulsion

Propulsion systems are an integral part of every spacecraft. They are necessary for delivery of the payload to its mission location, and for maintaining proper orbital location under the perturbing forces of the Sun and planets. Space propulsion generally includes both the launch vehicle used for leaving the Earth's surface, as well as any onboard propulsion used for orbit insertion and stationkeeping. Without reliable and efficient propulsion systems, exploration of the solar system and space beyond is not possible.

Space propulsion technologies can be divided into two general types: chemical and electric. Chemical propulsion relies on energy stored within the chemical bonds between atoms or molecules of the propellant. This energy is generally extracted through a combustion or reaction process, where the liberated excess energy produces a high pressure exhaust. This exhaust is expelled through a nozzle to create thrust for the satellite or spacecraft. Chemical thrusters can be bipropellant, where the mixing of two reactants starts the reaction and energy liberation process. Smaller chemical thrusters tend to be monopropellant and often have no chemical reaction involved, just utilizing stored energy in the form of tank pressure. These thrusters are typically referred to as "cold gas thrusters." Solid rocket motors are another type of chemical thruster where a solid propellant is burned, producing a high pressure exhaust. Chemical thrusters typically have specific impulses on the order of several hundred seconds. The most efficient chemical engine

built to date is the Space Shuttle Main Engine (SSME), which has a specific impulse of 465s in vacuum.

In contrast, electric thrusters can operate at much higher specific impulses than chemical thrusters. They rely on an external power supply to provide input power that is utilized in a variety of different ways, depending on the type of thruster. Electric thrusters typically come in three types: electrothermal, electrostatic and electromagnetic. Electrothermal thrusters operate in a similar fashion as chemical thrusters, except a heater is used to additionally increase the temperature of the propellant, thereby increasing the efficiency of the thruster. Electrostatic thrusters typically use a plasma discharge (Ion and Hall thrusters) or some sort of liquid propellant that can be easily ionized (Colloids, FEEPs). Thrust is produced by accelerating ions through electric fields. The specific impulse of electrostatic thrusters is only limited by the input power used to accelerate the ions. As more power is provided, the ions can be accelerated to greater velocities and specific impulse is increased. This theoretically has no upper limit (except the speed of light). Electromagnetic thrusters utilize both electric and magnetic fields to accelerate charged particles and produce thrust. These thrusters typically operate with a plasma discharge (MPD thrusters). Electromagnetic thrusters can produce relatively high thrust for an electric propulsion device, but their specific impulses are more limited than electrostatic thrusters.

These two main divisions in space propulsion technology represent two different operational purposes. Chemical propulsion is typically used for high-thrust maneuvers and has low fuel efficiency compared to electric propulsion. Launch vehicles use chemical propulsion systems because they produce the high thrust necessary for Earth escape. Electric propulsion is aimed more at low-thrust missions such as stationkeeping and orbit transfers where time to transfer is not the highest priority. Many forms of electric propulsion require a low density vacuum environment to operate and are thus precluded from launch vehicle use, where operations typically begin near sea level. The benefit of electric propulsion is seen in its fuel efficiency, which is often several times that of chemical rockets. As the onboard availability of power increases for spacecraft in the future, likely through

nuclear power technologies, higher power electric propulsion will become possible and the large gap in thrust between electric and chemical propulsion technologies will begin to close.

1.2 Hall Thrusters

Currently available Hall thrusters have specific impulses in a broad range of approximately 1500-3000s. The specific impulse range of Hall thrusters has recently been identified by NASA as very appealing for both stationkeeping and orbital transfer missions to the near planets [13]. Hall thrusters can be scaled to various sizes and powers relatively easily, with thrusters ranging from as small as 50W to over 10kW. Hall thrusters are also capable of throttling, changing their thrust and specific impulse by varying parameters such as discharge voltage and flow rate. This capability makes them ideal for missions where different types of maneuvers require different levels of thrust and efficiency. For example, in a mission to Mars there will be a long period of low thrust during transfer from geocentric orbit to areocentric orbit where fuel economy is most important. As a spacecraft approaches Mars, a relatively rapid deceleration may be necessary for Mars capture, and a high thrust, low specific impulse maneuver may be desired. A single Hall thruster might be able to perform both types of maneuvers in a single mission.

1.2.1 Description

Hall thrusters are plasma acceleration devices that utilize both electric and magnetic fields to produce thrust. The thruster geometry consists of an axis-symmetric, annular discharge chamber with an interior metallic anode and an externally mounted cathode. Propellant is injected at the anode and enters the discharge chamber at low velocity. An axial electric field is established between the positively charged anode at the back of the thruster and the negatively charged electron cloud produced outside the discharge channel by the cathode. A radial magnetic field is created by either permanent magnets or electromagnets placed around the annular channel and along the thruster centerline. This radial magnetic field is

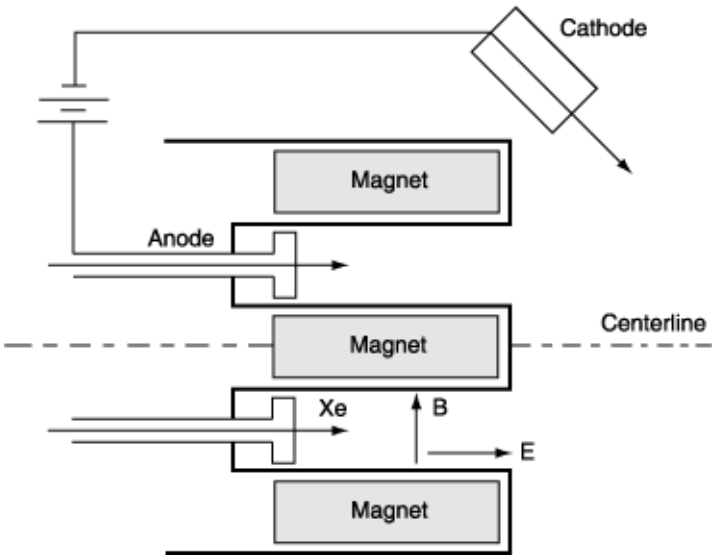

Figure 1.1 Diagram showing the Hall thruster geometry in cross section. The electric field is axial and the magnetic field is radial in direction.

one of the distinguishing features of Hall thrusters. A diagram of a Hall thruster is presented in Figure 1.1.

The magnetic field is strong enough to reduce the electron Larmor radius to a small value in comparison to the width of the discharge channel. Thus, the electrons are effectively trapped in azimuthal drifts around the annular channel as they slowly diffuse across the magnetic field towards the anode. The azimuthal drift current of electrons is called the Hall current. These trapped electrons serve several purposes. First, they promote ionization through collisions. An electron-neutral or electron-ion collision produces a heavy ion and an additional electron. The ion is accelerated out of the thruster by the axial electric field, producing electrostatic thrust. The new electrons produced in ionization are trapped by the magnetic field and promote further ionization. Secondly, the trapped electrons transmit thrust to the thruster body through a magnetic pressure force exerted on the electromagnets. As the electrons are electrostatically drawn towards the anode and gain velocity, they are quickly deflected and accelerated azimuthally by the strong magnetic field. The electrons transfer their axial momentum to the magnets of the thruster through

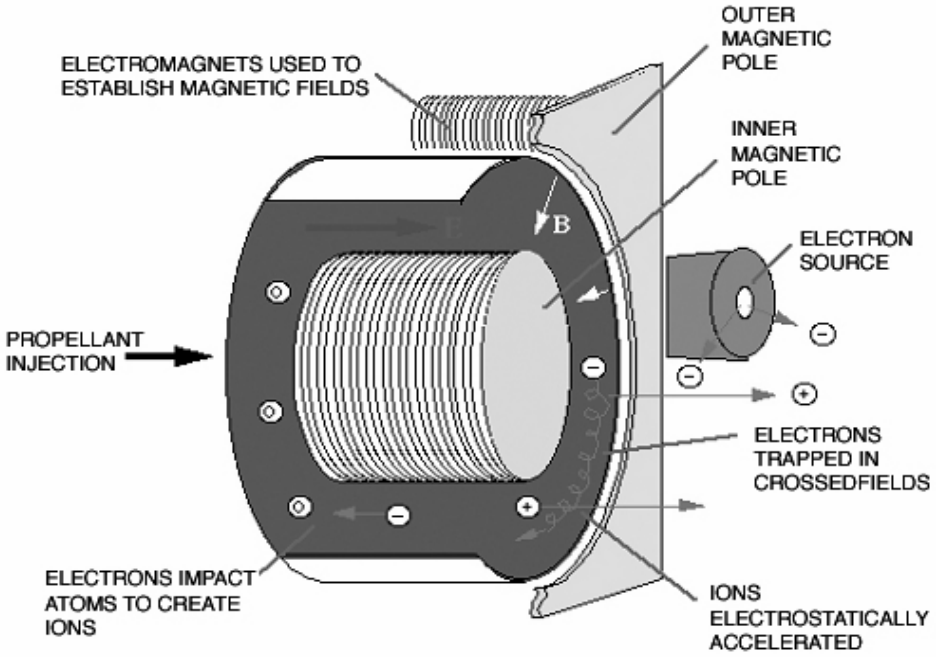

Figure 1.2 Schematic of a Hall thruster showing the significant mechanisms for ionization, electron trapping and thrust production. The azimuthal current of trapped electrons is referred to as the Hall current.

the magnetic field, creating a magnetic pressure force. The electron trapping mechanism, electron-neutral ionization and electrostatic acceleration of ions are all illustrated in Figure 1.2. It should be noted that the Hall thruster is still considered to be an electrostatic thruster because thrust is produced electrostatically through the acceleration of ions. The magnetic field is used only to confine electrons and transmit electrostatic thrust via the magnetic field. It is not used to accelerate charged particles as in an electromagnetic thruster.

Electrons originating at the cathode are also used for ion neutralization. The heavy ions ejected by the thruster can have hazardous charging and sputtering effects on a spacecraft or satellite. The damage can be reduced if the ions are effectively neutralized downstream

by cathode electrons. Furthermore, the cathode electrons help to maintain the axial electric field between the cathode and the internal anode.

The most common propellant used in Hall thrusters is xenon gas. Other propellants include argon, krypton and mixtures of air resembling the upper level Earth atmosphere. The main feature of a gas such as xenon is its high atomic weight. Xenon ions are unaffected by the thruster's magnetic field because of their large inertia, unlike the electrons which are easily trapped in Larmor gyrations. The heavy ions are efficiently accelerated out of the thruster with little deflection caused by the magnetic field. If the ions were significantly lighter, their curved exit trajectories would represent losses in thruster efficiency due to poor thrust vectoring. Furthermore, there is an inverse correlation between atomic mass and the cross section for ionization, so the ionization losses tend to be higher with lighter weight propellants.

1.2.2 Advantages

Hall thrusters have several advantages over other propulsion systems that make them attractive options for integration with spacecraft. Their high specific impulse allows for either significant weight savings in propellant or a dramatic increase in satellite lifetime. In contrast to functionally similar ion engines that require precise alignment and careful production of delicate acceleration grids, Hall thrusters are easy to build and assemble because of their simple annular geometry and use of commonly available materials. The operation of a Hall thruster is relatively simple compared to other propulsion systems, as there are no moving parts besides propellant valves. Advancements in Hall thruster lifetime are being made continually, with thrusters currently operating for more than 7000 hours before failure [18].

1.2.3 Issues

Despite their numerous advantages, several operational problems with Hall thrusters remain. The main factor limiting lifetime of Hall thrusters is erosion of the inner channel

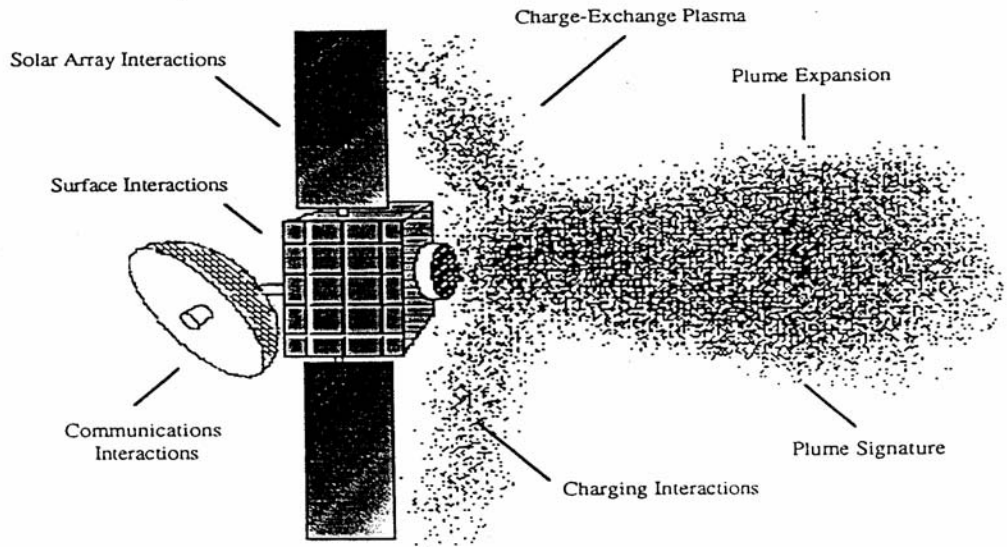

Figure 1.3 The plume of an electric propulsion system such as a Hall thruster can have damaging effects on spacecraft surfaces.

walls. Impingement from high velocity ions can sputter material from the channel walls, changing the wall geometry over time. Excessive electron heating can cause severe thermal stress and cracking of ceramic materials. Overheating can also affect magnet performance. Another important issue for spacecraft designers is the effect of the charged plume emanating from the thruster exit (see Figure 1.3). Spacecraft charging from backstreaming electrons and slow moving charge-exchange ions can be very damaging to delicate spacecraft surfaces such as solar arrays and communications antennas. Deposited layers of thruster exhaust material can form on various spacecraft surfaces, altering their thermal properties. Careful placement of the propulsion system is therefore required, and good modeling of the thruster's plume can provide important information for making these decisions.

1.3 Overview of Research

1.3.1 Previous Research

Research in Hall thrusters has been active for over forty years, beginning with their invention by the Soviet scientist A. I. Morozov in the early 1960's. Since their invention, over fifty Hall thrusters have flown on Russian satellites and research has flourished. Numerous analytical and computational models have been developed and experimental research has been plentiful. This brief review will focus on the most recent efforts of experimental research that closely relate to the research presented in this thesis.

Electrostatic internal probing of Hall thrusters has been performed by various researchers on a variety of different thrusters in recent years. At the University of Michigan's Plasmadynamics and Electric Propulsion Laboratory (PEPL), experimental research has been carried out on the P5 laboratory model thruster. Hass and Gallimore [1, 25] have used the High-Speed Axial Reciprocating Probe (HARP), a fast moving probe system that translates in and out of the internal discharge rapidly in order to ensure survival of the probe and minimize plasma disturbances. They have made axial profiles as well as radial-axial contour maps of plasma parameters in the discharge and the near exit region using both Langmuir and emissive probes mounted on the HARP system. Researchers at the Princeton Plasma Physics Laboratory (PPPL) have also performed experiments using both stationary and moving Langmuir probes, including characterization of plasma disturbances produced by these probes [2]. The research at Princeton was performed on a nine centimeter diameter Hall thruster built at the PPPL. Movable Langmuir probes have also been used in Israel to investigate axial profiles of plasma parameters in Hall thrusters [3].

There have been several experiments performed that closely resemble the Langmuir probe experiments presented in this thesis. They include work in Russia on a SPT-100 Hall thruster by Kim [4] and also on a SPT-50 in France by Guerrini [5]. A series of stationary, wall mounted Langmuir probes were placed inside the discharge channel in both experiments, and axial profiles of plasma parameters were determined at various operating con-

ditions. The experiment in France also used a movable probe in addition to the stationary probes.

The measurement of plasma parameters inside Hall thrusters is an important part of current experimental research. These types of measurements allow for comparison of different types of internal thruster geometries, as well as providing the physical insight necessary to construct accurate models of Hall thrusters. The data can also be used for verification of numerical and analytical models of the discharge physics. As the research progresses, the quality of models and physical understanding of Hall thrusters continually improves.

1.3.2 Motivation and Objectives

As research on Hall thrusters improves understanding of their underlying physics, design changes are proposed to increase performance and efficiency. Engineers typically make design changes on paper before manufacturing new parts, and then rebuild a thruster before performing a test of the new configuration under vacuum. The process of making design changes and testing under vacuum is both costly and time consuming. If numerical models were accurate enough to simulate the effects of design changes on thruster performance, design modifications could be "tested" without ever having to make a part.

A two dimensional, particle in cell (PIC) model originally developed at MIT by Szabo [6] is currently being used at the Busek Company as an aid in the design process. Design changes are implemented first in the code and further refined before new configurations are built and tested under vacuum. The original model is also currently being adapted to model the Michigan P5 thruster by Sullivan [7] at MIT. As the accuracy and reliability of PIC models continue to improve, they will play a larger role in the design process. However, a large part of developing any computational model is the verification of the model through comparison to experimental data. The main objective of this thesis is to provide accurate data for comparison with and verification of the PIC model used at the Busek Co. The secondary objectives are to increase the overall physical understanding of the internal

discharge characteristics of Hall thrusters and to provide data that can be scaled for comparison with models developed for other Hall thrusters.

1.3.3 Summary of Research

This thesis presents data collected and analyzed from June 2001 through June 2003. All testing was completed at the Busek Co. in Natick, MA using the Busek built BHT-1000 Hall thruster described in Chapter 2. Thruster performance data and results of some characterization experiments are also presented in the second chapter. Chapter 3 describes experiments performed using two different sets of axially distributed Langmuir probes. Plasma parameters were determined at various places inside the thruster to provide axial distributions of electron temperature, electron density and plasma potential for several different discharge voltages. Though most were internal probes, a few probes were also placed just downstream of the exit plane. In Chapter 4, the experimental data is compared to the predictions of the two dimensional PIC code. Chapter 5 contains concluding remarks and suggestions for future work.

Chapter 2

THE BHT-1000 HALL THRUSTER

The Busek built BHT-1000 Hall thruster was used for this research. It is a nominally one kilowatt thruster with a 68mm middle diameter discharge cavity. The thruster was originally developed at Busek under a Small Business Innovation Research (SBIR) program for high specific impulse operation, and its performance has been previously documented [8]. However, the thruster performance was retested for this research using an upgraded thrust stand and larger vacuum facility. The BHT-1000 can operate in both one and two stage configurations. Performance data were obtained in both configurations, while probe data were taken only in the single stage configuration. All testing was performed using xenon propellant.

2.1 Thruster Description

The laboratory model of the BHT-1000 measures 14.1x14.1x7.5cm and has a mass of 5.9kg, including the mass of the cathode and a small operating stand. The thruster is pictured without the external cathode and stand in Figure 2.1. There are four magnet coils around the outside of the thruster and one additional coil placed inside the center stem. The BHT-1000 was originally designed using scaling techniques to meet a performance objective of 3000s of specific impulse at 2300W input power while maintaining 100mN of thrust. Although the thruster has yet to meet this goal, it has been able to meet the specific impulse and power goals while maintaining 88mN of thrust [8]. The design has been pat-

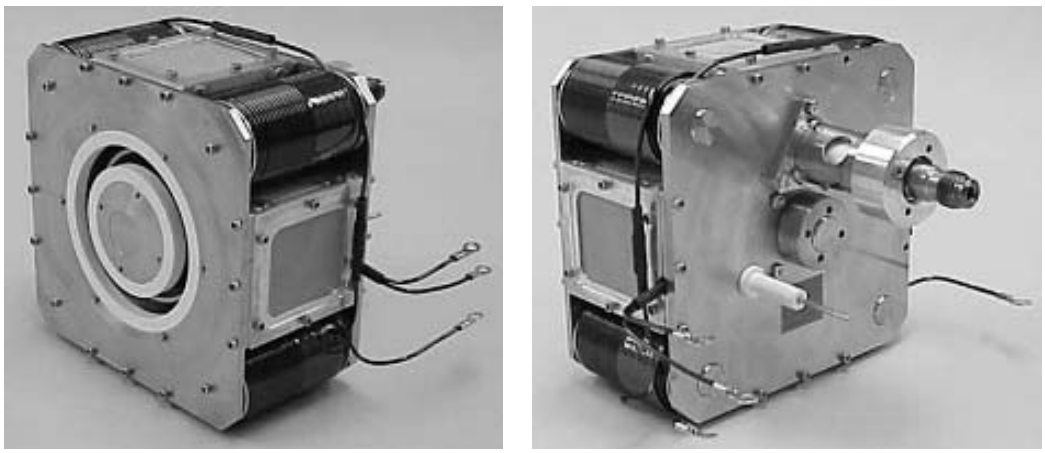

Figure 2.1 The Busek built BHT-1000 Hall thruster.

ented by Busek and has many distinguishing characteristics. The internal discharge chamber employs several important technological advancements that contribute to the thruster's high performance and also facilitate two-stage operation.

A diagram of the internal discharge chamber is presented in Figure 2.2. The design includes a two piece anode consisting of a wedge shaped annular piece inside an annular channel shaped piece. The inner piece functions as the propellant distributor. Xenon gas enters the thruster through a main line and is distributed by the wedge shaped anode piece through a set of large radial holes. The inlet holes are designed such that the propellant enters the discharge chamber with zero axial momentum. This promotes a long residence time for ionization and increases propellant utilization. The outer anode piece, usually referred to as the anode housing, has a relatively large volume that acts as a propellant reservoir to aid in propellent distribution and improve flow uniformity.

This composite anode allows the two separate pieces to be biased individually for two-stage operation. The inner anode is usually operated at the higher potential relative to the cathode, while the anode housing operates at an intermediate potential. The aim of two-stage operation is to physically separate the ionization and acceleration processes. Ionization is meant to occur in the upstream region between the highest and intermediate poten-

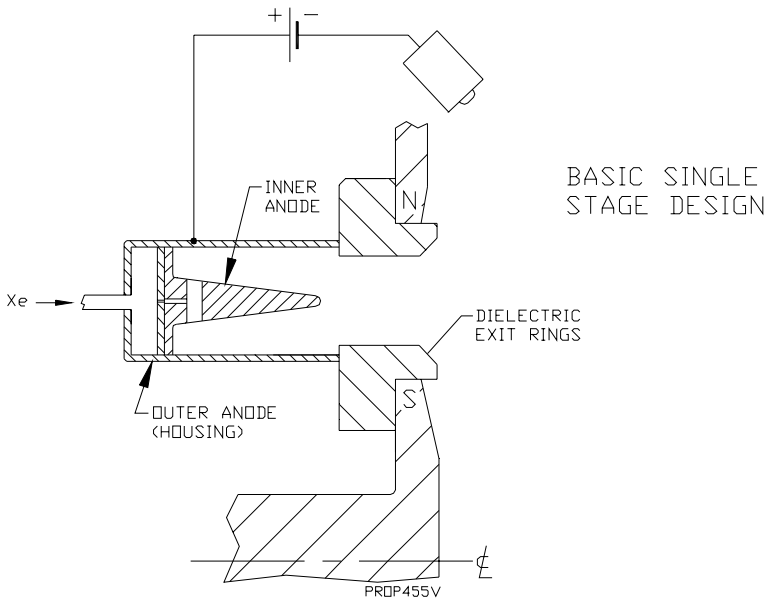

Figure 2.2 Diagram of the of BHT-1000 in cross-section.

tial, where the greatest density of propellant neutrals exists. Ion acceleration occurs closer to the thruster exit plane, between the intermediate electrode and the external cathode. This region is where the radial magnetic field is strongest, the neutral density is lowest and the electron density is large due to magnetic field trapping. If the ionization and acceleration mechanisms can be successfully decoupled, they can be independently controlled, leading to higher thruster efficiencies. The two-stage idea has been around since the 1970s, however it has yet to live up to its potential.

The magnetic materials pictured in Figure 2.2 (north and south magnetic poles) are made of Hiperco 50A alloy. This soft magnetic alloy is made mostly from iron, cobalt and vanadium. It has a higher saturation field, permeability and Curie point than magnetic iron, allowing for weight savings and a stronger radial magnetic field. The anode housing can also be made of a magnetic material and act as a magnetic shunt to help shape the magnetic field profile. The main effect of the shunt is to increase the axial gradient of the radial magnetic field and shift the maximum magnetic field magnitude further down-

stream. This shaping of the magnetic field helps minimize ion loss to the walls and has been shown previously to increase thruster performance over those with non-magnetic anode housings. By minimizing ion impacts of the dielectric walls, erosion is limited and ions are not wasted from a thrust vantage point, thereby increasing performance and lifetime of the BHT-1000 thruster.

The discharge chamber walls near the exit plane (exit rings) are made of a dielectric material, similar to the Russian Stationary Plasma Thruster (SPT) design. In SPT thrusters, these dielectric walls extend to the back of the thruster; however in the BHT-1000, the insulating wall material is concentrated near the exit plane where erosion is typically strongest. The dielectric used in the BHT-1000 is boron nitride, and both exit rings are built with a chamfer cut into them to preemptively account for a majority of the erosion found in SPT thrusters. The dielectric walls in SPT thrusters typically do not originally have chamfers, but erosion has been found to remove end material in previous testing at Busek. By removing this material beforehand, performance is more consistent over the life of the thruster.

The external cathode used with the BHT-1000 is the HCN-252 Hollow Cathode Neutralizer made by Ion Tech, Inc (pictured in Figure 2.3). It is a hollow thermionic emitter made from a material with a low work function. The exact material is not made clear by the manufacturer, but it is likely to be a material such as tungsten or tantalum, impregnated with barium oxide. This combination of materials emits electrons easily upon heating and by applying an electric field. The cathode flow rate is typically ten percent or less of the anode flow rate. The cathode steady state power consumption is low, generally on the order of 0-30W. Once the cathode is running and the thruster is started, the cathode power can be turned off and electron emission will continue unassisted. If the thruster is shut down or the plasma discharge goes out for any reason, the cathode discharge usually extinguishes as well. It is therefore advantageous to run a small amount of power through the cathode keeper so that the startup process need not be repeated in the event of a temporary thruster burnout.

Figure 2.3 The HCN-252 Hollow Cathode Neutralizer built by Ion Tech, Inc. is used with the BHT-1000.

2.2 Test Facilities

All testing was performed in Busek's T8 vacuum tank at their facility in Natick, Massachusetts (see Figure 2.4). The tank is made of stainless steel and measures 5m in length by 2.4m in diameter. The T8 uses a mechanical roughing pump, a blower, three two stage cryogenic pumps and five single stage cryogenic pumps capable of evacuating 180,000 l/s of xenon. The pressure inside the tank is typically close to $1x10^{-6}$ Torr before turning on the thruster propellant flow. During thruster firing, the pressure is always held below $1x10^{-5}$ Torr and usually operates near $6x10^{-6}$ Torr, depending on the propellant flow rate. There are thruster level viewing ports on both sides of the tank in the test section as well as two eye level viewing ports at the target end of the tank. The tank has a liquid nitrogen cooled target as well as a liquid nitrogen cooled shroud around the top part of the testing section.

The thrust stand used in the performance testing is of the inverted pendulum type originally developed at the NASA Lewis Research Center. The construction and calibration of the thrust stand are similar to those previously documented [11, 12]. The thrust stand uses a Schaevitz 050 HR Linear Variable Differential Transformer (LVDT) that measures dis-

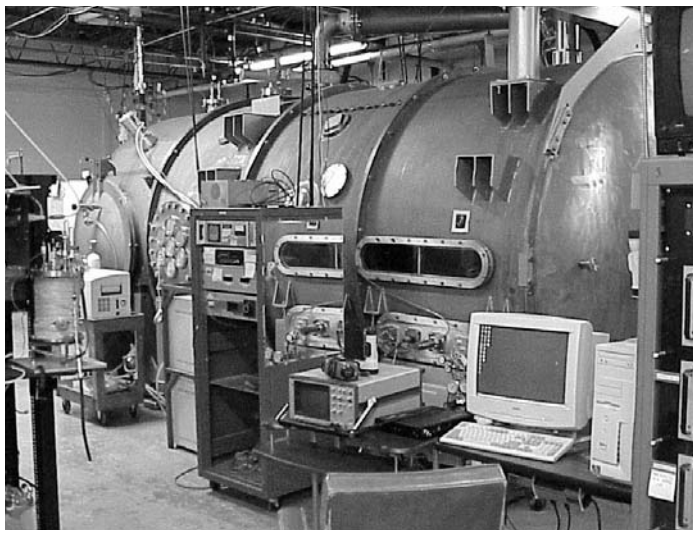

Figure 2.4 The Busek T8 vacuum test facility.

placement and produces an output voltage proportional to the thrust. The signal is read into a computer data acquisition (DAQ) card so that the thrust signal can be filtered and monitored using LabView software. The thrust stand is water cooled and can be calibrated in situ. Inclination of the thrust stand is read with an inclinometer and actively controlled with a leveling motor.

2.3 Thruster Operation

The general operating procedures for the BHT-1000 will be briefly reviewed here. Once the tank has been pumped down to the low 10^{-6} Torr level and the thrust stand has been calibrated, the propellant flow can be initiated. The cathode flow is started first at ten percent of the desired anode flow rate, generally in the range of 0.25-0.3 mg/s of xenon. After the cathode flow has been opened, there should be an allowance of 15-30 minutes for the cathode line to fill with propellant. Then, the cathode heater current should be turned on initially to 2A. The cathode element should be gradually heated by increasing the heater current by 2A every 10-15 minutes. The cathode heater current should not exceed 8A if possible. Once the cathode has been heated, the keeper voltage should be set at 300V to start the cathode discharge. If the cathode has trouble starting, higher voltage

can be gradually applied. Once the cathode starts, the heater current can be turned off, as the cathode will be self heating during operation. The keeper voltage can then be reduced to approximately 50V.

After the cathode has been properly started, anode flow can be initiated. The nominal anode flow rate is in the range of 2.5-3 mg/s of xenon. The discharge voltage can then be applied, starting at 300V. The thruster will start at lower voltages, but 300V has proven to be a good nominal starting condition. The anode current is typically very close to 2A at this condition, depending on the flow rate. A 40μF capacitor is usually used in the discharge circuit to minimize current oscillations. Once the thruster is started, the magnet currents controlling the electromagnets around the thruster can be increased. The inner and outer magnet currents are adjusted so as to minimize the discharge current, which will generally maximize thruster efficiency.

Initially after igniting the discharge, the plume is usually very fuzzy and expansive. A small, blue inner core jet can be seen, surrounded by a pink, spherical mass of background plasma, similar in color to the cathode plasma. Sometime during the first 30 minutes of warmup, the thruster will usually undergo a very sudden change into what is known as a "jet mode" plume configuration where the inner core jet is much larger and longer and the surrounding background plasma is significantly reduced. The thruster tends to run better in this warmed up state, with smaller discharge current oscillations and higher thrust. It is hypothesized that this transition could be due to an initial outgassing of the thruster surfaces, particularly the dielectric walls which can absorb moisture when not kept under vacuum. This phenomenon has been observed in previous research as well [9, 10]. The startup behavior with the pink, background plasma is more easily seen with the naked eye than in photographs. An attempt at a photographic comparison to the steady state jet mode is made in Figure 2.5. Note that the top photo has Langmuir probes mounted to the thruster, while the bottom photo does not. The pictures were taken during separate test firings of the thruster.

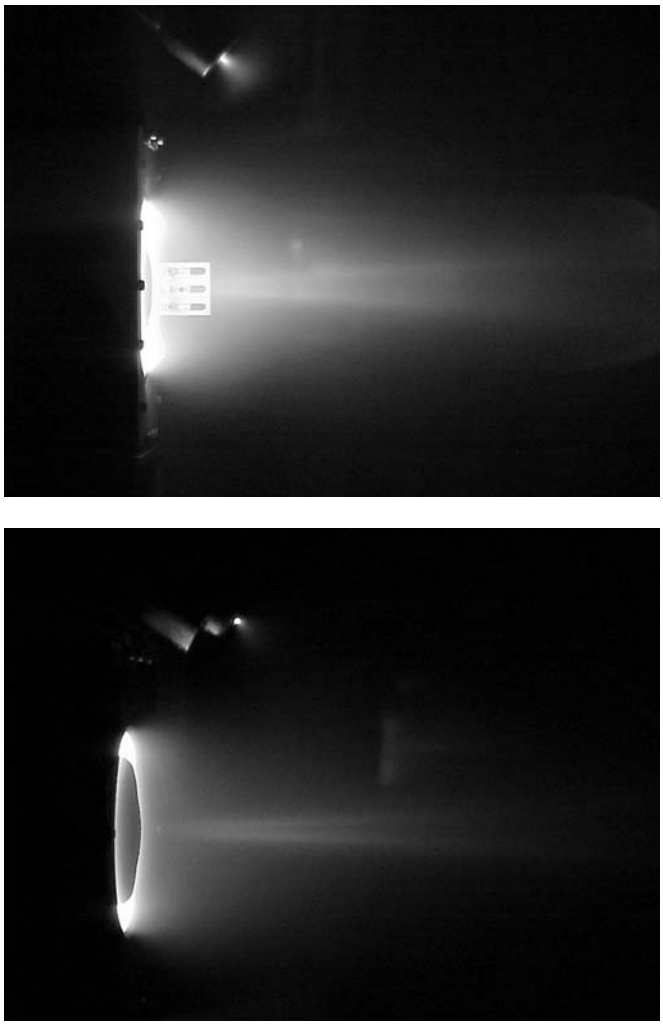

Figure 2.5 Comparing the initial thruster startup behavior to the steady state behavior. In the top photo, the thruster is seen with a pink, expanded plume and a wide jet. In the bottom photo, the warmed up thruster has a narrow spike and the plume is almost entirely blue in color.

2.4 Thruster Characterization

Additional testing was performed to characterize the thruster in conjunction with the performance testing. First, the magnetic field of the thruster was roughly mapped while the thruster was not firing, but the magnets were turned on. Secondly, a thermocouple was

buried within the outer boron nitride exit ring to determine the temperature during operation. These tests are described in more detail below, along with their results.

2.4.1 Magnetic Field Testing

The magnetic field test was performed for several important reasons. The inner magnet coil can get very hot due to the high thermal loads within the thruster during operation, and this can short the magnet wire if the insulation is damaged. By testing the magnetic field, the magnet operation could be verified. Additionally, the PIC model being used at Busek uses a magnetic field solved for by the Maxwell finite element software package. The results of the PIC code depend on the magnetic field used to model the thruster, so it needed to be verified experimentally. An axial-radial map of the magnetic field was made for comparison with the results of the Maxwell software. Furthermore, the Langmuir probes described in Chapter 3 are placed in an important part of the discharge channel. In order to verify that they were not disrupting the magnetic field, the azimuthal variation of the radial magnetic field around the channel was also tested.

Magnetic Field Test Setup

To make a two dimensional axial-radial map of the near probe region of the magnetic field, the thruster was placed on a translation table. A Gaussmeter probe was placed in a stationary position using a mechanical arm (see Figure 2.6). The translation table moved the thruster to different positions as the Gaussmeter data were recorded. Maps of the radial component of the field and the axial component were made separately because measuring each component required a different probe. The axial-radial field was mapped at two different magnet settings. The testing was performed with I_{inner}=2A and I_{outer}=4A as well as twice that setting, I_{inner}=4A and I_{outer}=8A. Data were taken at eight different axial positions, beginning at the tip of the anode and extending downstream. Eleven different radial positions were used in total. Due to the thickness of the probes in relation to the channel width, only three radial positions could be taken inside the main channel.

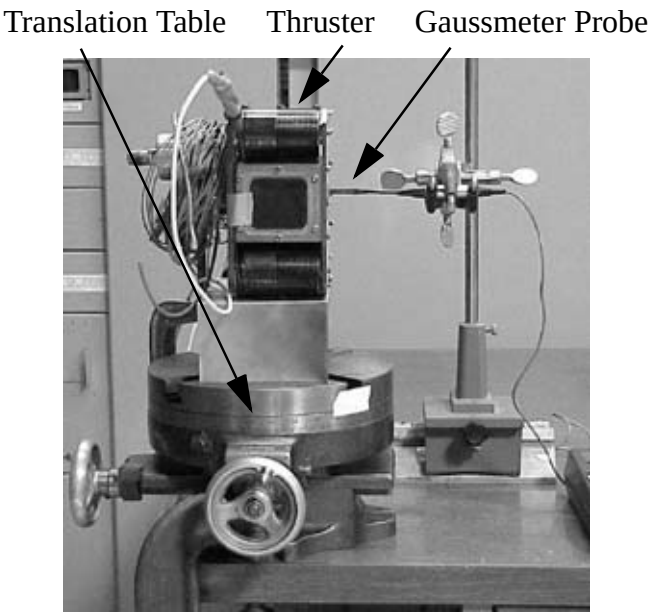

Figure 2.6 Side view of the axial-radial magnetic field test setup.

In order to test the azimuthal variation of the radial magnetic field around the annular discharge channel, a special mounting apparatus was built to hold the Gaussmeter probe. The probe could be placed inside the apparatus at three different axial positions and rotated around the channel while maintaining radial orientation. This mounting apparatus was affixed to the thruster during the testing, while the probe was rotated to take measurements every ten degrees around the discharge channel. The setup is pictured in Figure 2.7.

Magnetic Field Test Results

The data taken for the axial-radial map of the magnetic field were used to make contour plots of the field. The contour plots could were then compared side by side with the magnetic field computed by the Maxwell software package. Figure 2.8 shows that the experimental results match well with the Maxwell predictions. The data in these contour plots show the magnitude of the magnetic field in units of Gauss. The data shown in Figure 2.8 were taken with I_{inner}=4A and I_{outer}=8A. The contour map made with the experimental data lacks data points near the thruster walls, and therefore discrepancies in magnitude

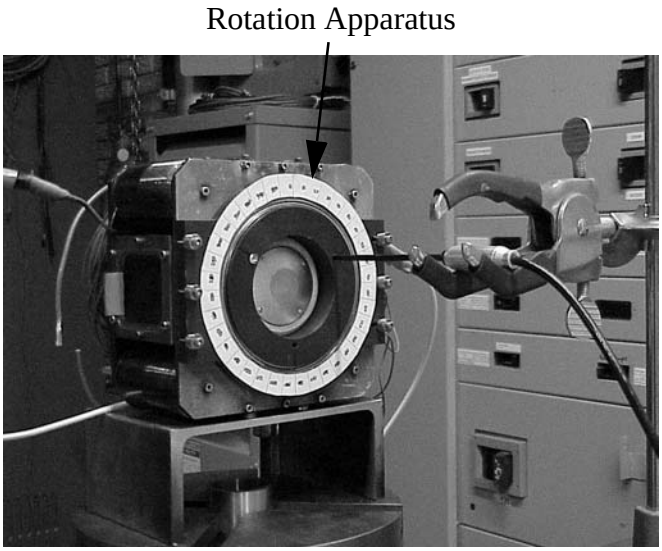

Figure 2.7 Setup to test the azimuthal variation of the radial magnetic field. A special apparatus was built to hold the Gaussmeter probe perfectly radial every 10 degrees around the discharge channel.

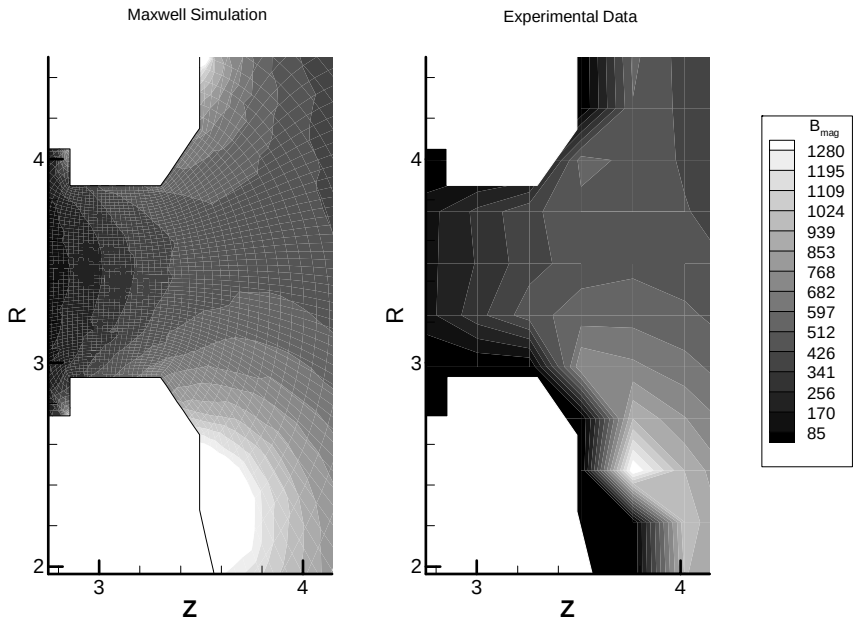

Figure 2.8 Comparison of the axial-radial contour maps of the magnetic field determined experimentally and using the Maxwell simulation. Position units are in (cm) and the magnetic field is in (G).

occur there. However, the magnitudes of the maximum field match well as do the overall magnitude profiles down the discharge channel.

The experimental data taken along an axial line at three different radial positions were compared to the simulation field along the same axial lines. The three radial positions correspond to those tested experimentally inside the main discharge channel. These radial positions are 32.3mm, 34.9mm, and 37.4mm measured from the thruster centerline. In Figure 2.9, the magnitude of the magnetic field measured along each of those lines is compared with that predicted by the simulation. The axial position is measured from the tip of the inner anode, and increases downstream. The data shown in Figure 2.9 were taken with I_{inner}=4A and I_{outer}=8A. Again, the agreement between experiment and simulation is good, showing that the magnetic field computed by the Maxwell software and used in the PIC simulations of the BHT-1000 is valid.

The azimuthal variation of the magnetic field was shown to be less than one percent for the three axial positions tested. In Figure 2.10, axial position one is furthest upstream, while position three is furthest downstream. All three positions tested were in the near exit plane region, and these data are from the testing done at I_{inner}=4A and I_{outer}=8A. The Langmuir probes discussed in Chapter 3 were located at 90 degrees. Because the measured radial magnetic field varied by less than one percent, it can be assumed that the presence of the probes did not significantly affect the magnetic field.

2.4.2 Thermocouple Measurements

When the BHT-1000 is operated at high power or at very high voltages (1000V and higher), the exit rings can overheat. This overheating may extinguish the discharge and potentially damage the thruster. Therefore, knowing the exit ring temperature is important for material selection and operation of the thruster.

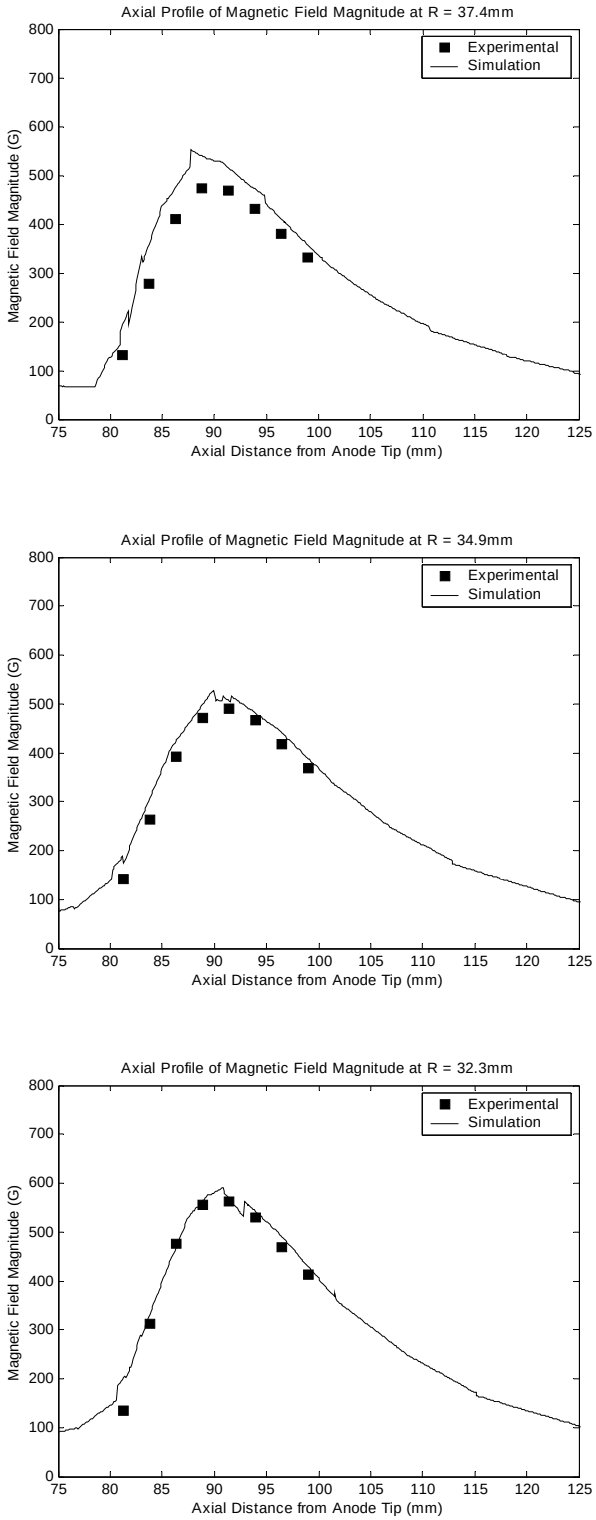

Figure 2.9 Comparing axial profiles of the magnetic field at three different radii.

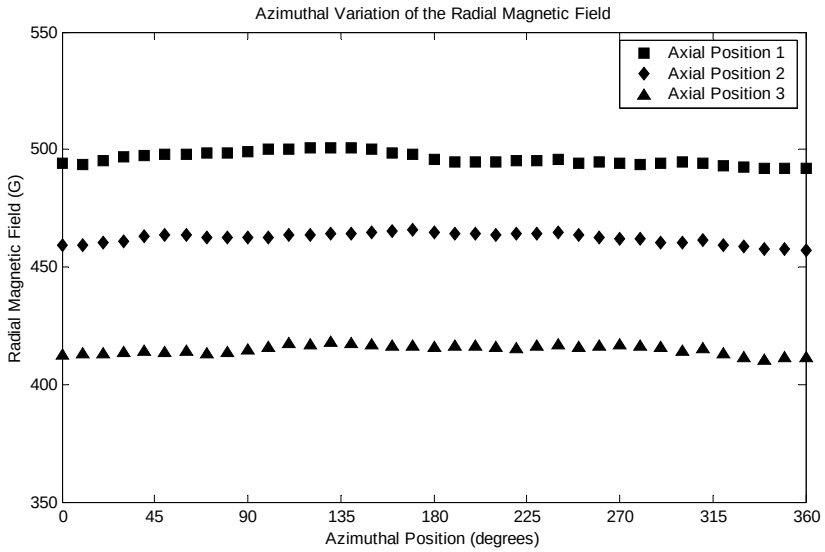

Figure 2.10 Plot of the radial magnetic field taken at three different axial depths and every ten degrees azimuthally around the channel. Position 1 is furthest upstream and position 3 is furthest downstream. Azimuthal variation was shown to be less than one percent.

Thermocouple Test Setup

To measure the exit ring temperature, a type K thermocouple was embedded in the outer exit ring. The thermocouple is run through a piece of dual-holed alumina tubing that is inserted from behind into a blind hole in the exit ring (see Figure 2.11). The tip of the thermocouple is located approximately 0.25in (0.64cm) radially outward from the ring surface adjacent to the primary discharge. Temperature was monitored and recorded during performance testing.

Thermocouple Test Results

The temperature of the outer exit ring was monitored in two separate ways. The first method was as the thruster warmed up from an off and cold state. This type of test was performed at flow rates of 2.0 mg/s and 2.5 mg/s of xenon, while the discharge voltage was held constant at 300V. The temperature of the exit rings increased steadily during the first hour or more of thruster operation (see Figure 2.12), and after two hours it began to level off and approach an equilibrium state.

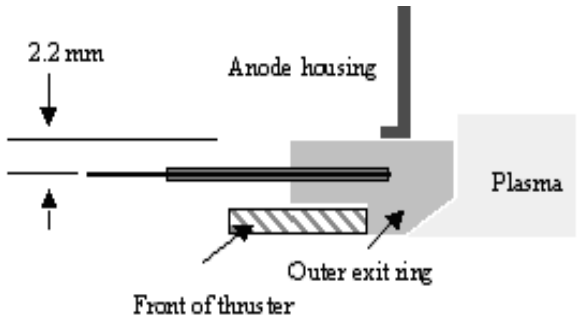

Figure 2.11 Cross section of outer exit ring with thermocouple embedded inside.

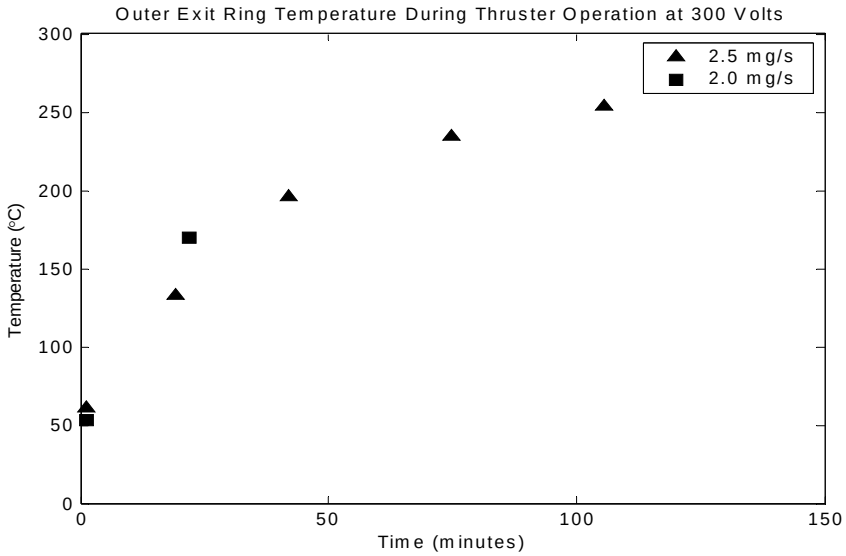

Figure 2.12 Measured temperature of the outer exit ring versus time the thruster has been running. Two sets of data were taken at on different days starting from a cold thruster.

The second type of test performed was to determine the maximum operating temperature of the exit ring at various discharge voltages. Figure 2.13 illustrates that the maximum temperature increases significantly with thruster discharge voltage. The maximum temperature measured at each voltage was a near steady-state value. Some voltages have several data points because the magnet currents were adjusted during testing and several data

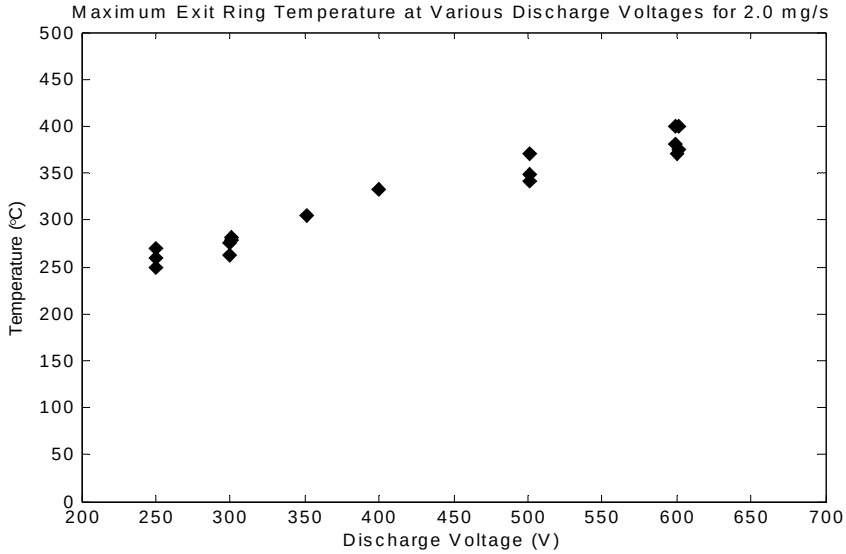

Figure 2.13 Measured temperature of the outer exit ring versus discharge voltage at an anode flow rate of 2.0 mg/s.

points were recorded. The thermocouple readout used during the testing was limited to 400°C, a point which was reached at a discharge voltage of 600V. It was also observed that when the discharge power was held constant, the exit rings overheated more easily at high voltage.

2.5 Performance Testing

Performance testing is an important component of both thruster design and modification. Baseline performance characteristics must be known in order to make comparisons to other thrusters and also for testing proposed thruster improvements. The BHT-1000 has been performance tested previously, and these data have already been published elsewhere [8]. The previous data were taken in a different, smaller vacuum facility at Busek. The larger test facility used for this new set of performance data is better suited for high and moderate power thrusters such as the BHT-1000. Minor thruster modifications and improvements to the test facilities have been made since these previous data were taken. Noise in the LVDT output has been reduced by using more appropriate thrust stand flex-

ures for the size of the thruster being tested and by filtering the output in the LabView software. Furthermore, calibration of the thrust stand has been improved by better incorporating the effects of thrust stand inclination and thermal drift.

2.5.1 Single Stage Testing

When the BHT-1000 is run as a single stage thruster, a single discharge power supply is connected between the anode and cathode. The cathode is allowed to float, and usually hovers between 15-20V below the facility ground. The electrical setup for the single stage configuration is pictured in Figure 2.14. Additional power supplies are required to heat the cathode, provide a potential for the cathode keeper, and run both the inner and outer electromagnets. The discharge can start at a potential difference as low as 50V, but the thruster is generally warmed up at a nominal operating voltage of 300V. After the discharge has been established at a particular operating voltage, the magnet currents are tuned to minimize the discharge current, which generally optimizes the thruster efficiency.

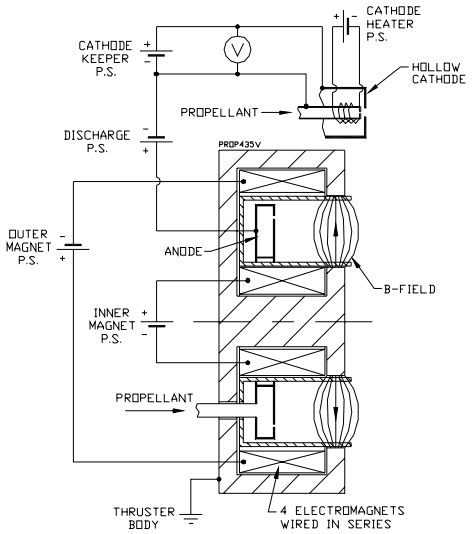

Figure 2.14 Electrical diagram for single stage testing of the BHT-1000.

The single stage testing was performed at four different xenon flow rates and voltages ranging from 300-1000V. The anode flow rates tested were 3.0, 2.5, 2.0 and 1.5 mg/s. The cathode flow rate was kept at ten percent of the anode flow rate. Data presented for thrust and discharge power are in raw form. Several data points appear at some voltages because the testing was done in overlapping sets, with some data points being repeated. Several measurements were also taken while tuning the magnet currents, which affects the discharge current and thrust. It is often advantageous to keep these data points separate in order to observe trends evolving over the test period; therefore, the points are not averaged. In Figure 2.15, it can be seen that the thrust increases with both discharge voltage and propellant flow rate. Higher voltages increase the propellant exhaust velocity because greater energy is imparted to the ions through the stronger electric field. In theory, thrust is linearly proportional to the exhaust velocity,

$$T = (\dot{m}_a c), \tag{2.1}$$

and the exhaust velocity depends on the voltage through,

$$c = \sqrt{\frac{2q_i\Phi_d}{m_i}}. \tag{2.2}$$

Thus, the thrust should increase with the square root of the discharge voltage. In the single stage performance data, the thrust does appear to level off at the higher voltages in a square root fashion, but only for the lowest two flow rates tested. The thrust measured at the higher flow rates seems to increase with discharge voltage in a near linear fashion. Higher flow rate increases thrust because more neutrals are available for ionization and acceleration. Hall thrusters tend to operate at high ionization fractions (nearly all neutrals are ionized), as evident in measurements of beam current. Plume research has shown that the measured beam current is typically near or greater than the discharge current, meaning that most (or all) neutrals in the discharge chamber are ionized [10].

As seen in Figure 2.16, the power consumption of the thruster also increases with voltage and flow rate. Higher voltage increases the flux of charged particles through the thruster,

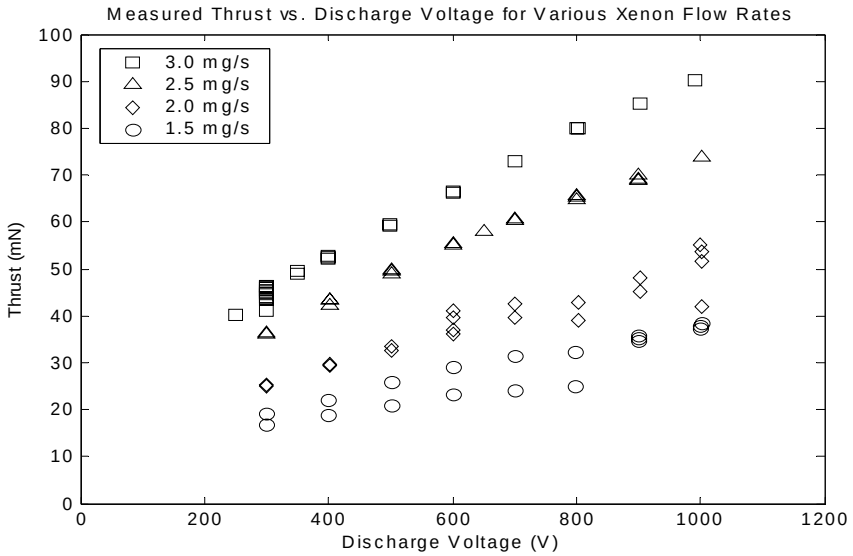

Figure 2.15 Plot of BHT-1000 measured thrust versus discharge voltage for various anode flow rates tested in the single stage configuration.

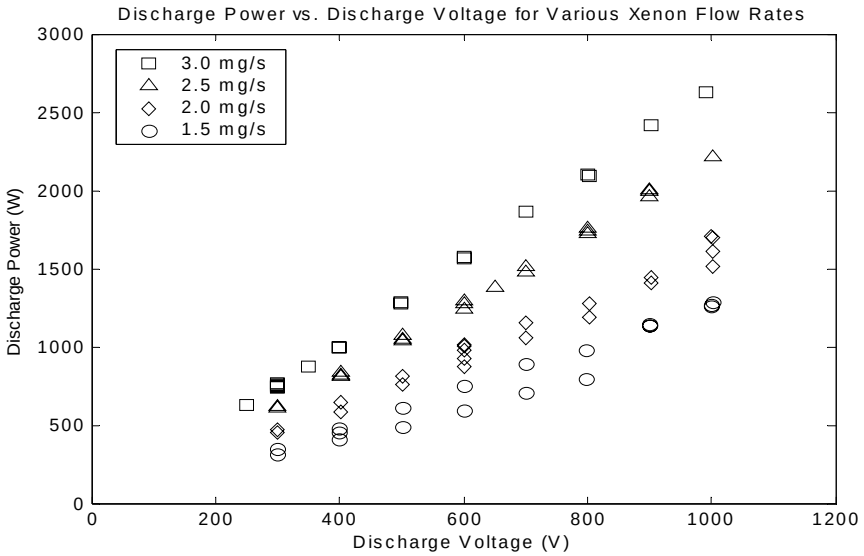

Figure 2.16 Plot of BHT-1000 discharge power versus discharge voltage for various anode flow rates tested in the single stage configuration.

thereby increasing the discharge current and power in a near linear relationship. Larger flow rates provide more neutrals for ionization, thus increasing the density of charged particles and subsequently the discharge current and power. It can be noted from Figure 2.16 that even though the BHT-1000 was originally designed as a one kilowatt thruster, it is capable of operating at much higher power levels.

The specific impulse is a type of fuel efficiency that evaluates the ability of the thruster to convert propellant into useful thrust and is defined as,

$$I_{sp} = \frac{T}{\dot{m}_a g}. \tag{2.3}$$

To make an electric propulsion system an attractive option for long duration solar system exploration missions, or even low Earth orbit (LEO) to geosynchronous Earth orbit (GEO) transfer missions, it typically needs to operate at specific impulses above 3000s. Only ion engines currently operate in this range of specific impulse. However, there is both motivation and effort underway to push the specific impulse of Hall thrusters into this range [13]. As previously mentioned, the BHT-1000 was designed for high specific impulse operation. Figure 2.17 shows that the thruster reaches a specific impulse of 3000s at 1000V for the largest two flow rates tested. The specific impulse data were averaged for this plot in order to reduce the scatter associated with the lower flow rates. At 2.0 mg/s and 1.5 mg/s, the discharge extinguished several times and had to be restarted, indicating that these flow rates were probably too low for steady operation. Furthermore, the plume was observed to be in the fuzzy, expansive mode for much of the performance testing at the lower two flow rates whereas the smoother, jet mode was observed consistently in the higher two flow rates. Another important point to note is that the specific impulse calculation only takes into account the propellant flow rate to the anode and does not include the cathode flow rate.

The thrust efficiency of the engine can be defined as the ratio of exhaust kinetic energy (also known as the beam energy) to input power. The beam energy is simply,

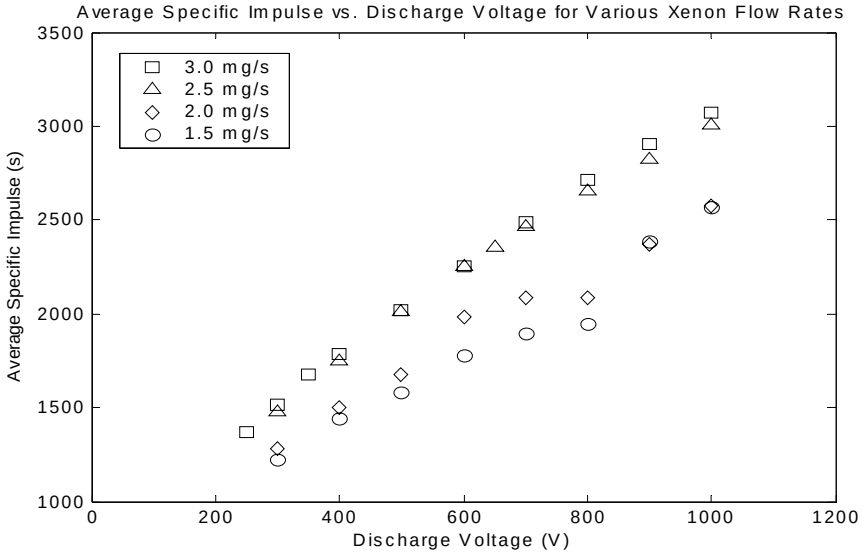

Figure 2.17 Plot of BHT-1000 average specific impulse versus discharge voltage for various anode flow rates tested in the single stage configuration.

$$E_{beam} = \frac{1}{2}\dot{m}_a c^2 . \tag{2.4}$$

The expression for efficiency can be reduced (using Equation 2.1) to parameters involving only the measured thrust, discharge current and engine inputs of anode flow rate and discharge voltage,

$$\eta = \frac{\frac{1}{2}\dot{m}_a c^2}{\Phi_d I_d} = \frac{T^2}{2\dot{m}_a \Phi_d I_d} . \tag{2.5}$$

As with specific impulse, the propellant flow rate used here is just the anode flow rate. Figure 2.18 shows the calculated efficiencies for the single stage performance testing. The thruster reached 50 percent efficiency at 800V for both the 2.5 mg/s and 3.0 mg/s flow rates tested. The data for these flow rates overlap, but both look as if they level off with increasing voltage. The lower flow rates are less consistent in their trends because of the erratic thruster behavior previously mentioned.

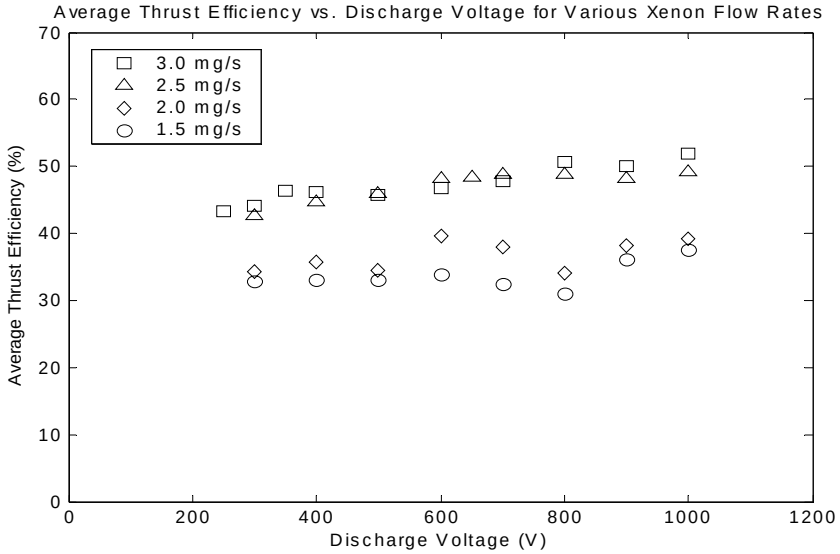

Figure 2.18 Plot of BHT-1000 average thrust efficiency versus discharge voltage for various anode flow rates tested in the single stage configuration.

2.5.2 Two Stage Testing

An additional power supply is required when running the BHT-1000 in the two stage configuration. This extra power supply is used to bias the intermediate electrode (the anode housing) to a potential between the anode and cathode, typically 100V below anode potential. The electrical configuration for two stage operation is shown in Figure 2.19. The magnet currents are tuned to minimize the discharge current, as in the single stage operation.

As previously discussed, the idea behind two stage operation is to physically separate the ionization and acceleration regions. By isolating these mechanisms, they can be independently controlled and tuned for higher efficiencies. Because the PIC simulation of the BHT-1000 does not yet fully incorporate this two stage configuration, only limited performance testing was completed with two stage operation. The performance of the BHT-1000 operating with two stages has been previously documented and shown to give a slight advantage in specific impulse, especially at very high power levels [8].

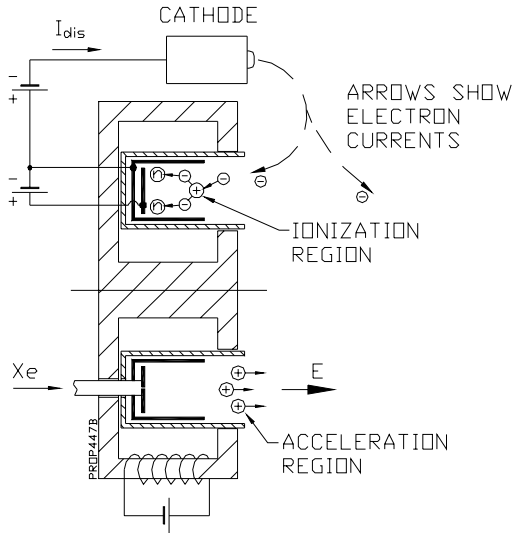

Figure 2.19 Electrical diagram for two stage performance testing of the BHT-1000.

The discharge is typically started using a potential difference between the anode housing electrode and the cathode. Once the plasma has been established, the extra voltage can be applied to the normal single stage anode above the electrode. The two stage data presented here used an anode flow rate of 2.0 mg/s. The cathode flow was kept at ten percent of the anode flow, as in the single stage testing. Figure 2.20 shows the thrust measured for the BHT-1000 operating in the two stage configuration as well as the single stage configuration for comparison. The voltage of the two stage data is the potential of the electrode and anode added together to get the total potential drop from anode to cathode. The plot shows that two stage operation gives a slight thrust advantage at this flow rate.

The total discharge power under two stage operation is plotted in Figure 2.21 along with the single stage data at the same flow rate. The two stage power consumption is calculated by adding the input powers to both the anode and intermediate electrode. The data show that two stage operation uses slightly more power to produce the higher thrust shown above. This increased power consumption may be because the intended ionization layer forms upstream between the anode and intermediate electrode, increasing the total ioniza-

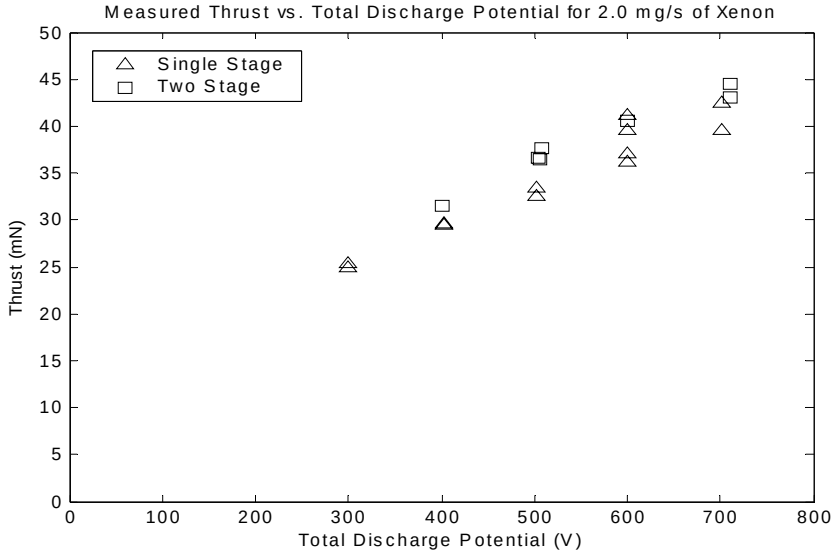

Figure 2.20 Plot of BHT-1000 thrust for single and two stage configurations at an anode flow rate of 2.0 mg/s of xenon. Two stage operation gives a slight thrust advantage at this flow rate.

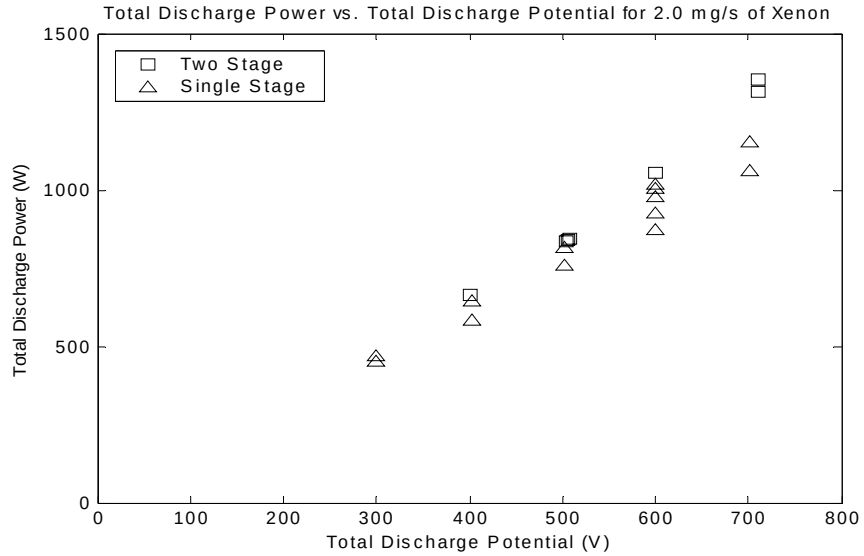

Figure 2.21 Plot of BHT-1000 power for single and two stage configurations at an anode flow rate of 2.0 mg/s of xenon. Two stage operation consumes slightly more power at this flow rate.

tion occurring inside the thruster discharge channel. If the ionization was not just moved upstream away from the acceleration layer as intended, but simply increased in amount by forcing it to occur both in the upstream region and near the exit plane, then an increase in total discharge current would be expected. This is because more electrons would be created by ionization and captured by the anode surfaces. This increases the total discharge current and therefore also increases the total discharge power.

The average specific impulse for two stage operation and the corresponding single stage data are plotted in Figure 2.22. The multiple electrode configuration performs better at all voltages tested. This improvement could be an effect of the physical separation of the ionization and acceleration zones. If accelerating ions encounter fewer neutrals downstream, charge exchange collisions are less likely. Charge exchange collisions occur when a fast ion collides with a slow neutral. The neutral takes on the charge of the ion and becomes a slow ion while the original impacting ion loses its charge and becomes a fast neutral. This type of collision translates to a thrust and specific impulse loss because the slow charge exchange ions cannot overcome the radial potential gradient of the plasma and diverge away from the main thrust axis.

The comparison of single and two stage thrust efficiencies is complicated by the poor operation of the single stage configuration at this flow rate. The two stage operation did not have problems at 2.0 mg/s, so a definite advantage exists in discharge stability. The average measured thrust efficiency for two stage operation is clearly as high as the single stage configuration, but the trend at higher potentials is difficult to determine without further testing. Again, because of the possible increase in ionization with the two stage setup, it is likely that higher discharge power and electron current will lead to inefficiencies. It should be noted that in the case of two stage operation, the input power in the denominator of Equation 2.5 (used to calculate the thrust efficiency) is the sum of the powers consumed by both discharge power supplies.

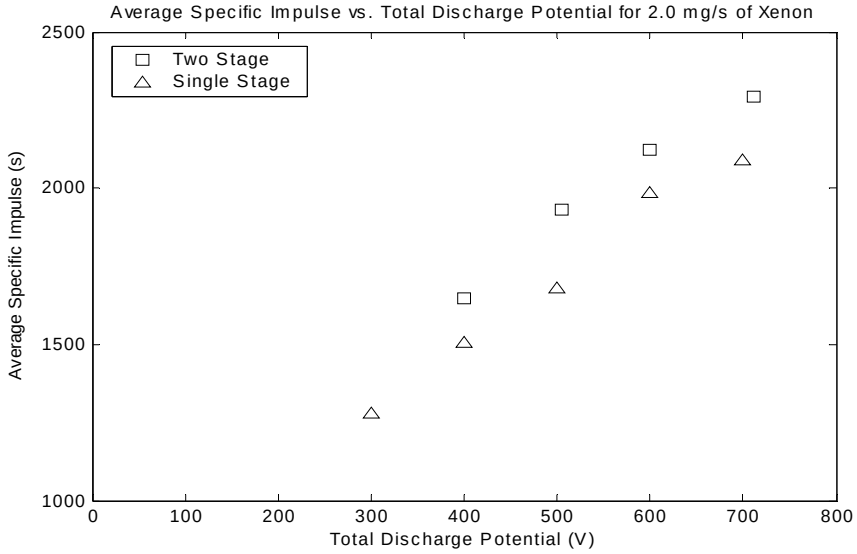

Figure 2.22 Plot of BHT-1000 specific impulse for single and two stage configurations at an anode flow rate of 2.0 mg/s of xenon. Two stage operation performs at a higher average specific impulse at this flow rate.

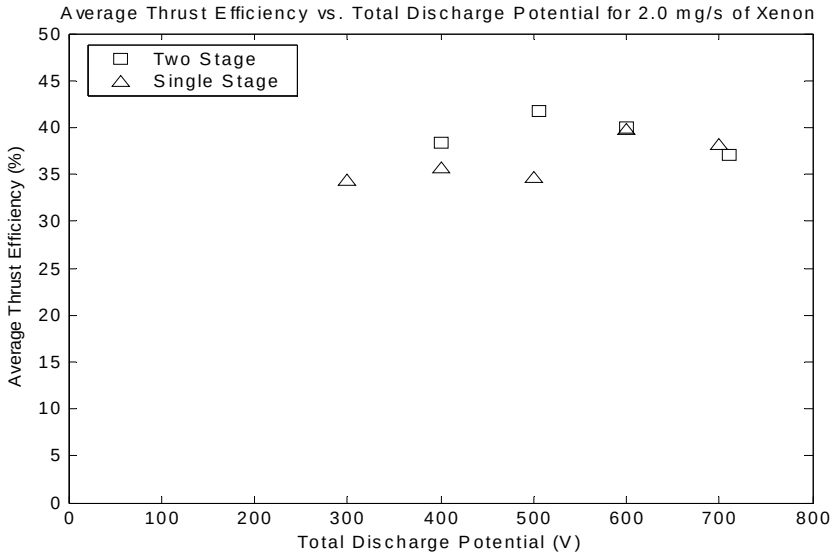

Figure 2.23 Plot of BHT-1000 thrust efficiency for single and two stage configurations at an anode flow rate of 2.0 mg/s of xenon.

Chapter 3

INTERNAL PROBE MEASUREMENTS

3.1 Overview of Langmuir Probes

Electrostatic plasma probes were invented by the scientist Irving Langmuir in the year 1924. His relatively simple devices were the first plasma diagnostic instruments and still bear his name, as electrostatic probes are most commonly referred to as "Langmuir probes." They are capable of measuring electron density, ion density, electron temperature, plasma potential and floating potential. Their accuracy in measuring these plasma properties depends on the particular situation in which they are used. Their use is limited to cool plasmas which will not melt or rapidly erode their surfaces because they are material probes that must be inserted into the plasma. Despite their simple construction and operation, the interpretation of their data can be quite complex [14].

3.1.1 Simple Langmuir Probes

Langmuir probes generally consist of one or more metallic, conducting electrodes inserted into a plasma. The "simple" Langmuir probe is a single electrode where one conductor is inserted into the plasma. All of the Langmuir probes used in this research were of this type. A grounded power supply is used to bias the probe to potentials both above and below the plasma potential, while the current collected by the probe is measured. Figure 3.1 shows a schematic of a simple Langmuir probe on the left. The probe is a conducting wire typically made out of a high temperature metal such as tungsten or nickel,

and is surrounded by an insulating sleeve, usually made out of a ceramic such as alumina. The conductor extends out of the insulator some distance to form the probe area.

The right hand side of Figure 3.1 shows a schematic of a voltage-current sweep of a simple Langmuir probe in a stationary, Maxwellian plasma. As the probe potential is swept across a broad range of voltages and the current collection is measured, a characteristic curve with three distinct regions is extracted. Each of these regions allows one or more of the plasma parameters to be determined.

The current collected by the Langmuir probe in Figure 3.1 is the sum of both electron and ion currents arriving at the probe. Figure 3.2 illustrates current collection regimes of the probe corresponding to each of the regions shown in Figure 3.1. Note that current leaving the probe is typically regarded as positive, while current collected (as in the ion saturation region) is plotted as negative on the voltage-current sweep. At very low potential, the probe attracts all of the surrounding ions and repels all but the very high energy electrons (far right of Figure 3.2). This region of the voltage-current sweep is called the ion saturation region because the current is relatively constant, as the maximum flux of ions allowed by space charge considerations is collected. The ion saturation region is used to determine the ion density.

As the probe voltage is increased, the potential gradient between the plasma and the probe decreases and more electrons reach the probe. Eventually, electrons and ions arrive at the probe in equal rates, causing the total current to the probe to be zero (second image from right of Figure 3.2). This potential is called the floating potential and is denoted as V_f in Figure 3.1. Increasing the probe voltage still further, the electron current begins to dominate the total current collected by the probe because the lightweight electrons are easily diverted from the surrounding plasma. This region on the probe characteristic is referred to as the transition region, and the electron current increases exponentially with probe voltage (second image from left of Figure 3.2). The slope of the transition region can be used to determine the electron temperature.

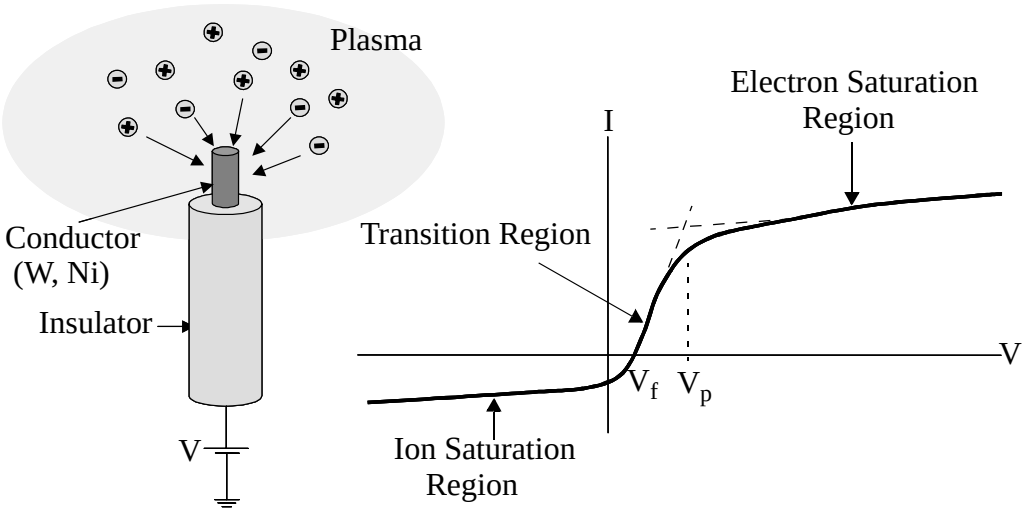

Figure 3.1 Schematic of a Langmuir probe is shown on the left, collecting ions and electrons from a plasma. A diagram of the basic Langmuir data curve appears on the right.

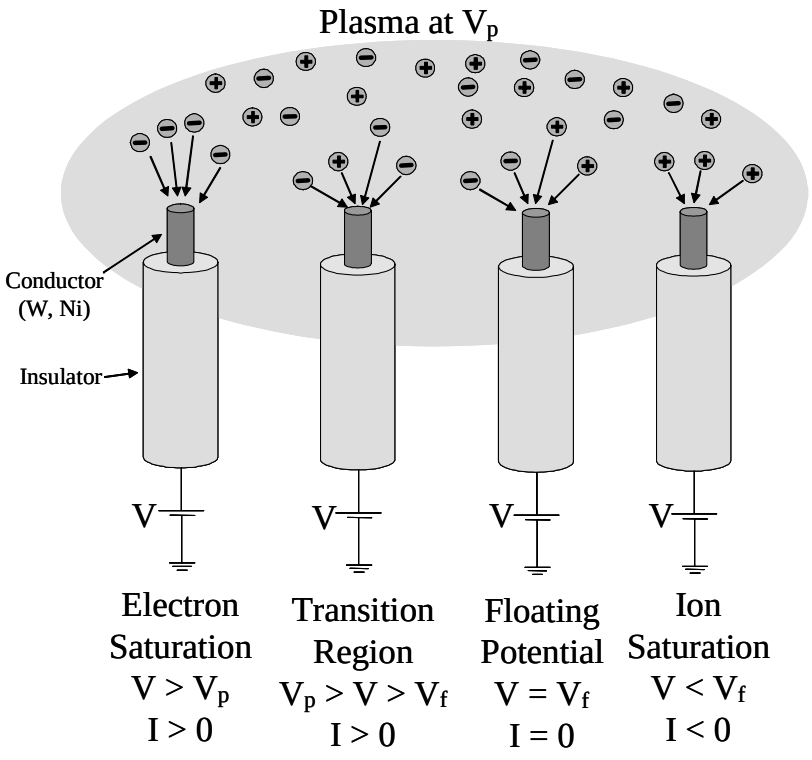

Figure 3.2 The different collection regimes of the simple Langmuir probe are illustrated by four separate Langmuir probes in this concept diagram.

As the probe voltage approaches the plasma potential (V_p), the ion current is completely diminished and the electron current begins to saturate. When the Langmuir probe is operating in the thin sheath regime (this will be discussed in more depth), a kink or knee will appear in the curve at the plasma potential. The region of higher potential beyond the plasma potential is referred to as the electron saturation region and is used to determine the electron density (far left of Figure 3.2).

3.1.2 Multiple Electrode Langmuir Probes

When two electrodes are used, referred to as a "double" Langmuir probe, they are inserted into the plasma near each other so that they sample the same plasma properties. Both electrodes are initially floating at potentials below the plasma potential. A power supply is connected between the two electrodes so that a potential difference can be applied between the two electrodes. The potential difference is varied using the power supply, while the current between the probes is recorded. The main advantage to using a double Langmuir probe instead of a simple Langmuir probe is that there is only a very small net current drawn from the surrounding plasma, keeping plasma disturbances to a minimum. The current to the double Langmuir probe is constrained by the fact that the current collected in one electrode must be taken from the other electrode. Thus one end of the system is always limited to drawing the ion saturation current at maximum, which tends to be a very small current. However, the disadvantage of the double Langmuir probe is that it cannot be used to determine the floating or plasma potentials. It can be used for determining the electron temperature and the plasma density (from the ion saturation current).

Triple and quadruple Langmuir probes have also been used in plasma research. These probes typically use one electrode as a reference potential (allowed to sit at the floating potential) and bias the other electrodes to fixed potentials above and below the reference point. Then analytical curve fitting is used to determine the plasma parameters from the three or four known points on the probe characteristic. This allows for all of the important plasma parameters to be determined without sweeping the probe bias, but the disadvan-

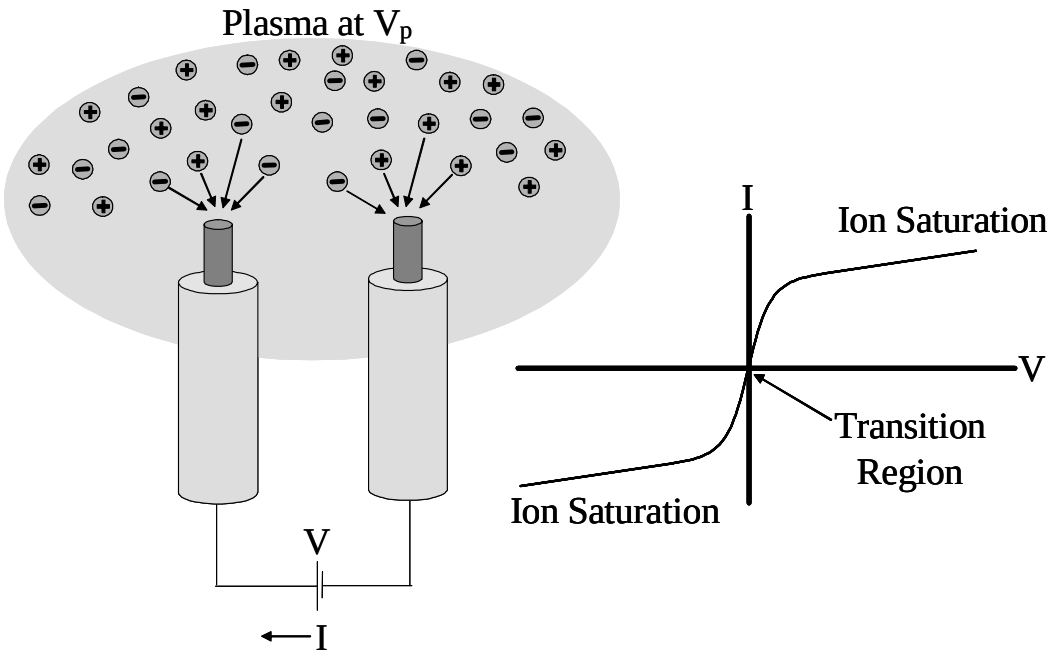

Figure 3.3 The double Langmuir probe concept uses two electrodes with a biasing power supply connected between them. Plasma disturbances are minimized, but plasma potential cannot be determined using this type of probe.

tage is that the probe size and complexity become greater with each electrode added. These types of probes can be valuable for plume research and other types of external diagnostics, but they are cumbersome for performing internal discharge measurements on all but the largest Hall thrusters.

3.2 Simple Langmuir Probe Theory

Classical Langmuir probe theory for single electrode probes relies on a few assumptions about the plasma environment in which the probe is placed. First, the plasma must be stationary and quiescent. The plasma should not be flowing due to external electric fields or confined by magnetic fields. Secondly, the plasma must be isotropic and Maxwellian, meaning that there is no preferred direction of flow or nonneutral density regions. Third, the plasma should be collisionless. The criterion for a collisionless plasma in this regard is that the mean free path is much greater than the probe dimension (usually radius) and the

Debye length. Finally, the probe must be operating in the thin sheath regime, meaning that the probe dimension must be much greater than the Debye length.

The Debye length is a plasma property that can be used to quantify the size of the electric potential boundary layer between the main plasma and its surroundings and is given by,

$$\lambda_d = \sqrt{\frac{\varepsilon_o k T_e}{e^2 n_e}}. \tag{3.1}$$

The potential of the main plasma will be relatively constant across large regions of uninterrupted quiescent plasma. However, near walls or physical objects within the plasma, the potential falls off from the plasma potential to the floating potential in a distance that is typically a few times the Debye length as illustrated in Figure 3.4. The region of potential drop is referred to as the "sheath" and the potential of the plasma at the entrance to the sheath is called the "sheath potential" (denoted by V_s). When the Debye length is an order of magnitude or more smaller than the probe dimension, the sheath can be assumed to be thin in comparison to the probe. This allows for the assumption of a planar probe geometry (no matter what the probe shape is) and edge effects may be ignored. This concept is illustrated in Figure 3.5.

When all of the classical Langmuir probe theory assumptions can be met, the interpretation of the probe characteristic becomes as straightforward as possible. The floating potential can be read directly from the voltage-current sweep as the potential where zero net current is collected by the probe. The ion saturation current is then determined from the ion saturation region of the characteristic and subtracted from the total current, leaving a plot of only the electron current. The electron temperature is then determined from the slope of the logarithm of the electron current in the transition region,

$$\frac{d \ln I_e}{dV} = \frac{e}{k T_e}. \tag{3.2}$$

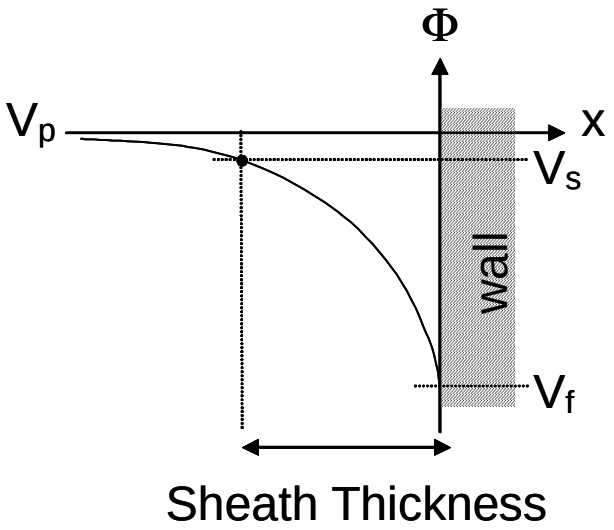

Figure 3.4 This diagram illustrates the concept of the potential sheath that exists between the plasma and physical objects within or around the plasma. The sheath thickness is typically a few times the Debye length.

Thin Sheath Criterion:

$\lambda_d / R << 1$

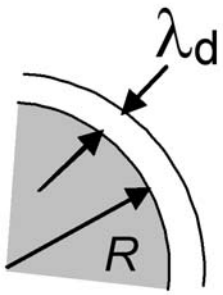

Figure 3.5 The thin sheath criterion requires that the Debye length be much smaller than the major probe dimension (usually the radius for a cylindrical wire). This ensures that edge effects can be ignored and the geometry can be considered to be planar.

Once the electron temperature has been calculated, the ion density can then be found using the ion saturation current and the area of the probe,

$$n_i = \frac{(I_i)_{sat}}{\exp\left(-\frac{1}{2}\right) A_p e v_B}, \tag{3.3}$$

where the Bohm velocity (v_B) is calculated from,

$$v_B = \sqrt{\frac{kT_e}{m_i}}. \tag{3.4}$$

In the Bohm velocity equation, the ion mass term would be for a xenon ion since that was the propellant used in this research. Alternatively, the ion density can be found from the electron saturation current (see below) and quasineutrality (n_i=n_e). The plasma potential can be determined graphically from the kink in the characteristic. This can be done either on the raw data plot or using the logarithm plot of the electron current where the kink is more apparent. In the transition region, the electron current rises exponentially therefore appears linear on the logarithm plot of electron current. The plasma potential can also be determined using the floating potential and electron temperature from,

$$V_f - V_p = \frac{kT_e}{2e}\left[\ln\left(2\pi\frac{m_e}{m_i}\right) - 1\right], \tag{3.5}$$

which reduces to the following when using xenon as the propellant,

$$V_p = V_f + 5.76T_e. \tag{3.6}$$

This method for determining the plasma potential can be very valuable when the kink used in the graphical method is difficult to see. Once the plasma potential is determined, the electron saturation current is determined as the electron current measured at the plasma potential. The electron saturation current can then be used to determine the electron density from,

$$n_e = \frac{4(I_e)_{sat}}{e\bar{c}A_p}, \tag{3.7}$$

where $\bar{c}$ is the mean thermal speed of the electrons and is found from,

$$\bar{c} = \sqrt{\frac{8kT_e}{\pi m_e}}. \tag{3.8}$$

Many resources about classical Langmuir theory are available, and much study has been devoted to its uses and applications [14, 15, 16, 17]. Analytical solutions to the current drawn by a Langmuir probe can be used to fit curves to the data and numerically derive the plasma parameters. This method can be a rapid and powerful tool for analyzing Langmuir probe data. However, a more manual method was used in this research as a way of better understanding and interpreting the nuances of the experiments.

3.3 Langmuir Probe Data Analysis

There are several practical considerations to make when trying to apply the simple Langmuir probe theory to experimental data. When any of the classical Langmuir probe assumptions are violated or when the experimental setup is flawed, departures from the nominal probe characteristic occur. This type of data is not without value, in fact it is very difficult to find practical applications in which none of the traditional assumptions are violated. Therefore, a review of the application techniques of Langmuir probe theory used in this research will be presented below.

3.3.1 Thin Sheath Procedure

When the probe characteristic looks similar to the type of curve expected under thin sheath assumptions, the data analysis is relatively straightforward. Figure 3.6 shows a plot of Langmuir probe data taken inside the BHT-1000 during an experiment. The characteristic looks as it should, with a clear ion saturation region, transition region, plasma potential kink and electron saturation region.

When the ion saturation region is enlarged, it is easy to see the floating potential where zero current is measured (see Figure 3.7). It is also easy to see that the ion saturation current is not truly a constant value. The current linearly increases in magnitude as the probe voltage is lowered further and further below the floating potential. This phenomenon occurs because the sheath surrounding the probe is growing as the potential difference between the plasma and probe is increased. Therefore, the effective collection area of the probe grows, and the ion current increases. It is therefore not obvious what value should be used for the ion saturation current in the data analysis.

For this research, the ion saturation current was chosen as the current where the linear region of ion saturation current stopped and the transition region began (marked by exponential growth in electron current). This ion saturation current was chosen because it mirrors the method of choosing the electron saturation current at the plasma potential kink (where electron saturation begins) and because it was found to give the most linear transition regions on the logarithm plots of electron current. This choice of ion saturation current also makes sense from a kinetic perspective. As the probe approaches the regime pictured in the far right image of Figure 3.2, the ions begin to dominate the current collected by the probe. At lower probe potentials, the flux of ions only increases because of sheath growth, not because ions are dominating the current collected in greater fractions compared to electrons.

Figure 3.8 shows an example of the logarithmic plot of electron current used to calculate the electron temperature and plasma potential. Both the transition region and the electron saturation regions are fitted with linear extrapolations. The slope of the transition region is used to find the electron temperature, while the intersection of the two extrapolations is used to determine the plasma potential. The current measured at the plasma potential is selected as the electron saturation current and from this, the electron density can be found. If the electron saturation was perfect and sheath growth did not occur, the electron saturation region would be flat instead of sloping upwards. However, as the probe voltage is driven above the plasma potential, the collection area increases due to growth of the

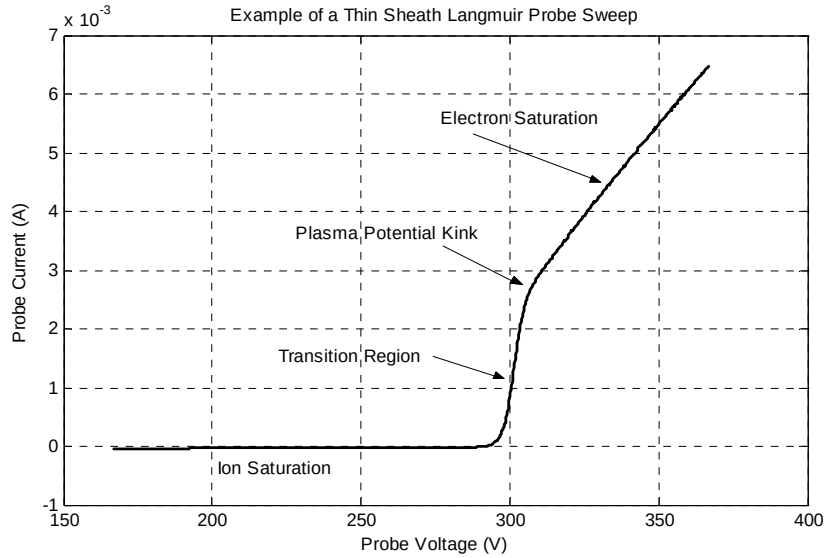

Figure 3.6 Example of a Langmuir probe sweep under thin sheath conditions. The plasma potential kink can easily be seen.

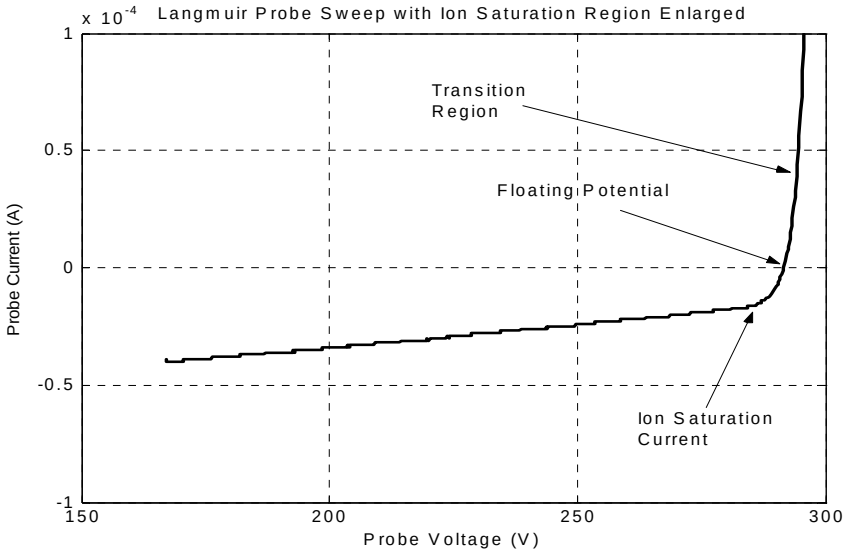

Figure 3.7 Enlarged view of ion saturation region of a Langmuir probe sweep under thin sheath conditions. The ion saturation current magnitude increases linearly as the probe voltage is decreased because of sheath expansion. The value used in data analysis is at the end of the linear region as shown.

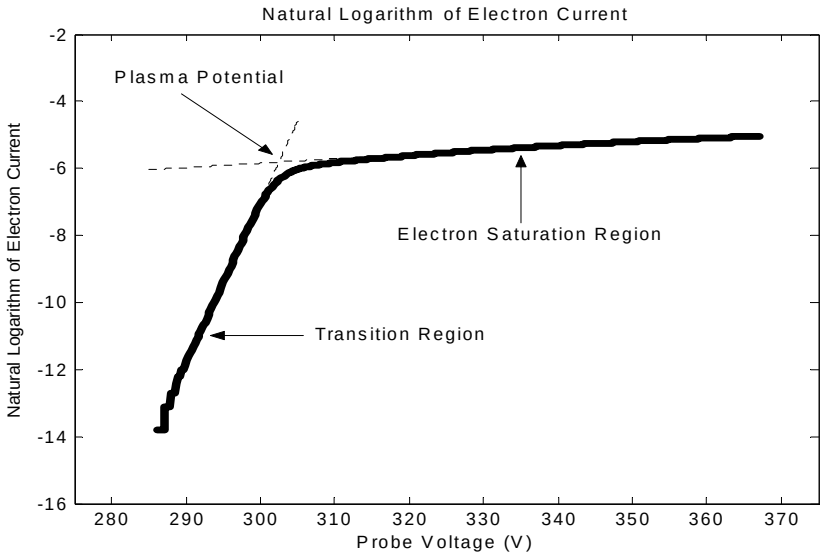

Figure 3.8 Plot of the natural logarithm of the electron current for a Langmuir probe sweep performed under thin sheath conditions. The plasma potential kink is even more pronounced here than in the linear plot of total current in Figure 3.6.

potential sheath surrounding the probe. This behavior is the same as previously discussed regarding growth of the ion saturation current with decreasing probe voltage.

3.3.2 OML Procedure

When the thin sheath criterion is violated, a Langmuir probe may operate in what is referred to as the Orbit Motion Limited (OML) regime. This regime occurs when the Debye length is much larger than the probe dimension ($\lambda_d >> R_{probe}$), meaning that the sheath thickness is large compared to the probe dimension. This effectively increases the size of the collection area by many times or even orders of magnitude. As the probe voltage is increased beyond plasma potential, the electron current will rise monotonically as the sheath grows in size. If the sheath grows in all directions, indicating a three dimensional OML regime, the rise in current will be linear. This would apply to a spherical Langmuir probe. If the sheath grows only in two dimensions (2D OML for a cylindrical probe), the electron current will rise with a square root dependence on the probe voltage. An infinitely planar Langmuir probe would show a perfectly flat electron saturation cur-

rent, as in the theoretical thin sheath case. However, because of the edge effects associated with a planar probe of finite dimensions, the growth of the sheath cannot be strictly planar in shape. A small planar probe would collect current from an unknown sheath shape, making the electron saturation region of the characteristic have some type of undefined curvature [16]. Oftentimes the Debye length is not much larger than the probe dimension, but rather on the order of the probe dimension ($\lambda_d \sim R_{probe}$). Under this type of condition, the probe can have behaviors that are intermediate between the thin sheath and OML regimes. This type of probe condition can be difficult to analyze because the proper assumptions are unclear.

In practice, the electron current never truly saturates (as seen in Figure 3.6), even when the conditions are determined to be in the thin sheath regime. However, the behavior of an OML (or intermediate) probe is dramatically different in the electron saturation region of the characteristic, and the data analysis must be modified. Figure 3.9 illustrates the difference in shape of the Langmuir probe characteristic between the OML and the thin sheath regimes. Although practical probe applications rarely approach true electron saturation, the thin sheath approximation is a useful technique in cases where the plasma potential kink is visible (Case C in Figure 3.9). However, when the probe is operating in the OML regime, no kink is visible and the plasma potential must then be solved for using Equation 3.6. It should be noted that this method of solving for the plasma potential is less reliable than the graphical method using the kink in the characteristic. This method requires that the floating potential and electron temperature be known beforehand. Determination of the floating potential is not difficult as it can be read straight from the raw data plot. Conversely, finding the electron temperature can be more challenging, as it is not clear where the transition region ends in the OML characteristic. It is known that the transition region typically encompasses the floating potential, so the electron temperature is therefore determined from the slope of the logarithm of electron current near the floating potential.

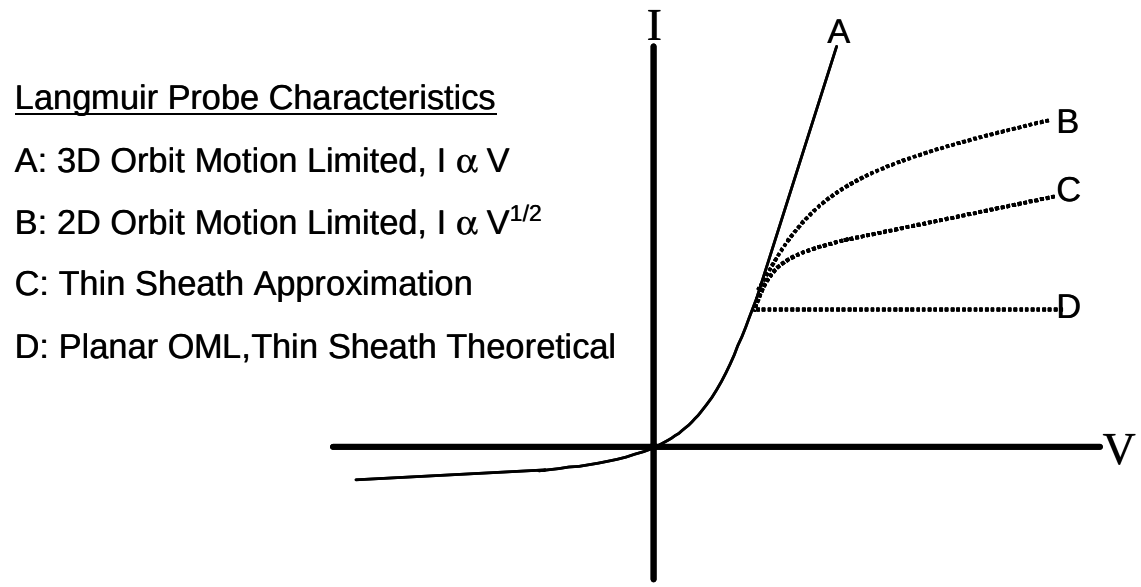

Figure 3.9 This diagram shows the difference in shape between the OML and thin sheath Langmuir probe characteristics. The theoretical thin sheath curve (D) is not typically found in experiments, but the thin sheath approximation (C) can be made when the plasma potential kink is clearly seen. Planar OML is also not observed in experiment because edge effects tend to be important on the scale of practical probe sizes. The typical OML cases (A, B) do not allow for graphical determination of the plasma potential.

3.3.3 Leakage Current Procedure

The considerations discussed so far in applying the simple Langmuir probe theory have focused on situations in which the thin sheath assumptions are violated. Another cause of aberrations in the probe characteristic is a flawed experimental setup. Because Langmuir probes are operated in a plasma environment where there is a constant background gas containing ions and electrons, electrical insulation of the non-current collecting areas is very important. The leads that carry the probe signal through the thruster body and to the edge of the vacuum tank must be shielded from this background gas. However, the interior of the thruster can be an extreme environment for normal insulating material. Heat is conducted through the probe itself to insulating materials that cover the probe and its signal carrying leads. Rubber insulation tends to melt, leaving exposed regions of wire that are biased at approximately the same potential as the probe itself. These exposed wires can attract and repel ions and electrons from the background just as the probe does in the

discharge plasma, leading to extraneous currents that affect the probe data and shift the curve from its true position.

Several types of insulation were utilized during this research. Rubber insulation of many thicknesses melted, likely due to a combination of heat conduction from the probe and electron heating. Ceramic wire insulations tended to crack at wire bend points, exposing probe leads. High temperature alumina putty and Kapton were found to be effective insulators. When data were affected by insulation problems, corrections were made to salvage the information about plasma properties. Because electrons in the background gas are more mobile than background ions, electrons more easily penetrate gaps in insulation. As a result, probes with insulation problems typically showed excess electron current and shifted the entire probe characteristic upwards.

Figure 3.10 shows an example of a leakage current correction made to a Langmuir probe sweep. The ion saturation region of the curve has been enlarged so that the correction method can be studied. The curve of measured current crosses the zero current line in a linear fashion typical of the ion saturation region of the probe characteristic, not with the exponential rise of electron current as in the case without leakage currents. In order to correct the plot, a current shift calculated using Equation 3.6 had to be applied. First, the plasma potential was solved for graphically using the kink in the probe characteristic (not shown in Figure 3.10). In order to do this, the ion saturation current had to be estimated visually. This estimation was done through a trial and error process of studying the natural logarithm plot of the electron current and estimating the ion saturation current until the plot of the transition region was as linear as possible. The linearity indicates that the plasma was Maxwellian, one of the major assumptions in applying classical Langmuir probe theory. Second, an estimate of the electron temperature was made from the slope of the same plot. Using Equation 3.6, these two parameters (V_p and T_e) were then used to determine a new floating potential. Once this had been done, the current shift downwards could be calculated by determining the amount of shift necessary to bring the new floating potential point to the zero current level. This process could then be iterated by making a

new estimate of the ion saturation current, recalculating V_p and T_e, and finding the floating potential from Equation 3.6 until it converged to a final value. A second iteration was rarely necessary, and a third correction has never been needed in this research.

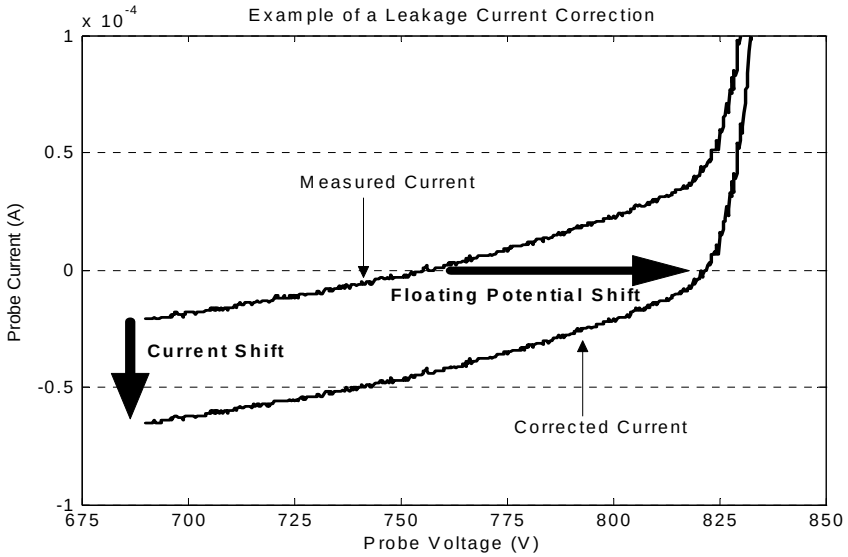

Figure 3.10 Example of a probe sweep with leakage current. The measured curve must be shifted down by solving for the correct floating potential. In this example, the floating voltage increased by 64.75V and the current decreased by 44μA.

3.3.4 Flowing Plasma Considerations

When a Langmuir probe is operated in a flowing plasma, a wake can be created behind the protruding probe as in Figure 3.11. Ions moving past the probe do not enter the wake because of their large inertia and high velocity. Electrons are therefore also prevented from entering the wake region because of quasineutrality. The wake region can complicate the determination of the probe collection area because it is difficult to quantify the effect of the wake on the sheath shape. Previous research on cylindrical probes aligned perpendicular to the flow direction has used the assumption that the ion collection area is determined only by the projected area of the probe. The electron collection area is assumed to be one half of the total surface area of the probe because electrons typically

exhibit more isotropic trajectories than ions [18]. Analytical solutions for current collection of cylindrical probes operated in flowing plasmas have been developed previously [14]. These analytical solutions can be numerically fitted to data to derive plasma properties.

This research utilizes planar Langmuir probes, which are less vulnerable to wake region concerns. However, Hall thrusters are flowing plasma environments where isotropic plasma assumptions are not completely accurate. Nevertheless, this research did not attempt to make corrections for plasma flow, as its complexity for planar probes was beyond the scope of this work.

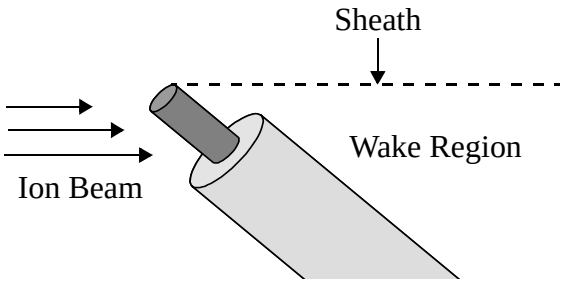

Figure 3.11 When a Langmuir probe is inserted in a flowing plasma, a wake region of low density can be created.

3.4 Langmuir Probe Experimental Setup

The placement of diagnostic instruments inside Hall thrusters of small or moderate size can be complicated for several reasons. The discharge chamber is typically very small, on the order of a few centimeters long in the axial direction and a couple of centimeters in radial width. Little space is left for the insertion of diagnostic instruments, especially because the anode occupies a significant portion of the volume within the discharge chamber. The insertion of diagnostics is further complicated by small, difficult to reach access pathways through the assembly. Many materials within the thruster are conductors and are often biased to high potentials, creating the possibility of short circuits and data cor-

ruption. Finally, the plasma within the discharge chamber typically has peak temperatures of 20eV and higher. These high temperatures can erode or overheat surfaces of diagnostic instruments that are left in the plasma during thruster operation.

3.4.1 Probe Design

To ensure the survival of the internal Langmuir probes for thruster test durations of many hours, the probes were designed to be planar probes placed flush with the surface of the ceramic outer exit ring. The ceramic exit ring is made of boron nitride and acted as the probe insulation near the plasma discharge. The probes were designed to be inserted from the outer radial surface of the exit ring and to be connected to lead wires inside the thruster body. These lead wires were ported through the side of the thruster and then to electrical feedthroughs on the side of the vacuum tank. A diagram of the probe design is shown in cross section in Figure 3.12.

The diameter of the probes was chosen to meet several different requirements. The probes were made of 99.95 percent pure tungsten and needed to be inserted through a small diameter hole approximately one half inch in length. Because the boron nitride was acting as the probe insulator, the diameter of the insertion hole was drilled to be very close in size to the diameter of the wire for a tight fit. Due to a high friction insertion, the wire needed to be stiff enough not to bend. In order to use the thin sheath probe theory, the probe diameter had to be large relative to the Debye length inside the thruster. Because the plasma parameters were not known beforehand, they were estimated using the PIC simulation. The initial estimate of Debye length, along with the estimated plasma parameters used to calculate it, are presented in Table 3.1. Also presented in the table are estimates of both the ion and electron saturation currents. It was important to estimate these current limits to ensure that the power supply used to operate the probe could handle the amount of power collected by the probe. The ion saturation current was estimated using Equation 3.3, and the electron saturation current was estimated using Equation 3.7. In using these

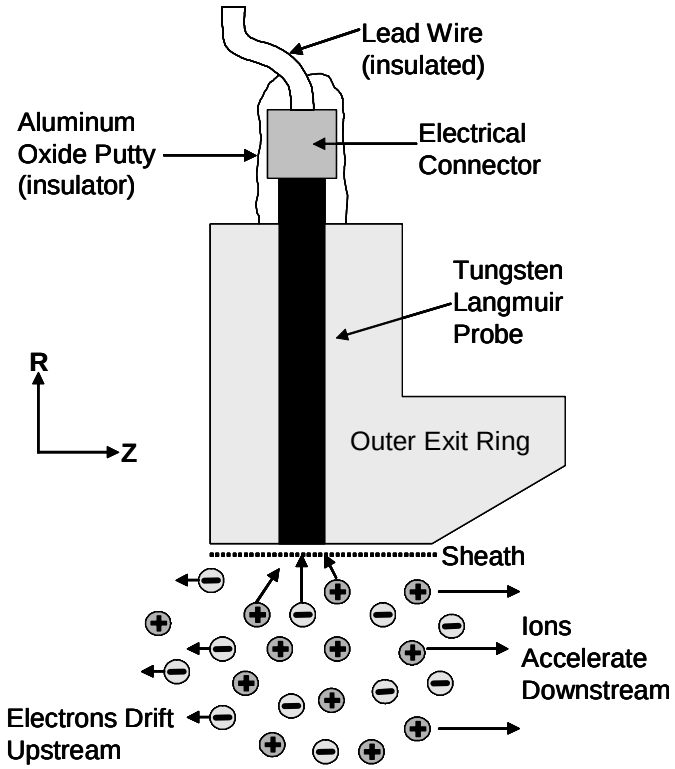

Figure 3.12 Diagram of Langmuir probe design shown in cross section. This diagram is not drawn to scale.

TABLE 3.1 Initial Estimates Used for Probe Design

Design Parameter	Initial Estimate
R_{probe}	2.54×10^{-4} m
n_e	3×10^{18} m^{-3}
T_e	20 eV
$(I_e)_{sat}$	72.78 mA
$(I_i)_{sat}$	0.23 mA
λ_d	1.9×10^{-5} m
R_{probe}/λ_d	13.22

equations, it is assumed that the probe operates in a thin sheath regime and that the ion temperature is much less than the electron temperature.

Initial estimates showed that a probe diameter of 0.020in (0.508mm) would be large enough to operate in a thin sheath regime, yet small enough that the electron saturation current would be below the power supply maximum (100mA). This diameter also provided enough stiffness for insertion through the narrow probe holes in the boron nitride.

3.4.2 Probe Construction

Once the initial probe diameter was selected, the locations for probe insertion were chosen. Previous research using electrostatic probes inside Hall thrusters has shown that the plasma properties tend to change rapidly near the exit plane of the thruster [1]. Probes were therefore spaced as evenly as possible throughout the axial distance of the outer exit ring, while making sure that at least one probe was placed near the upstream edge of the exit ring chamfer and one probe directly on the chamfer. The beginning of the chamfer forms the exit plane for the main discharge channel, and the end of the chamfer represents the end of the discharge channel altogether. It was hoped that by placing the probes near these exit plane areas, the large axial variations in plasma parameters would be captured by the probes.

Both experimental setups described below used eight Langmuir probes axially spaced as shown in Figure 3.13. The probes are often referred to by number and are ordered from one to eight moving downstream as shown. The first four probes were located on the internal discharge chamber surface facing radially. The fifth probe was located approximately midway down the exit ring chamfer, while the last three probes were mounted externally to the thruster. It is important to also note that probes 1-5 were spaced apart azimuthally as well to avoid any probe to probe interaction because of their small axial spread. The three external probes were mounted in double bored alumina tubing where one hole in each insulation tubing was not used. These external probes were not spaced

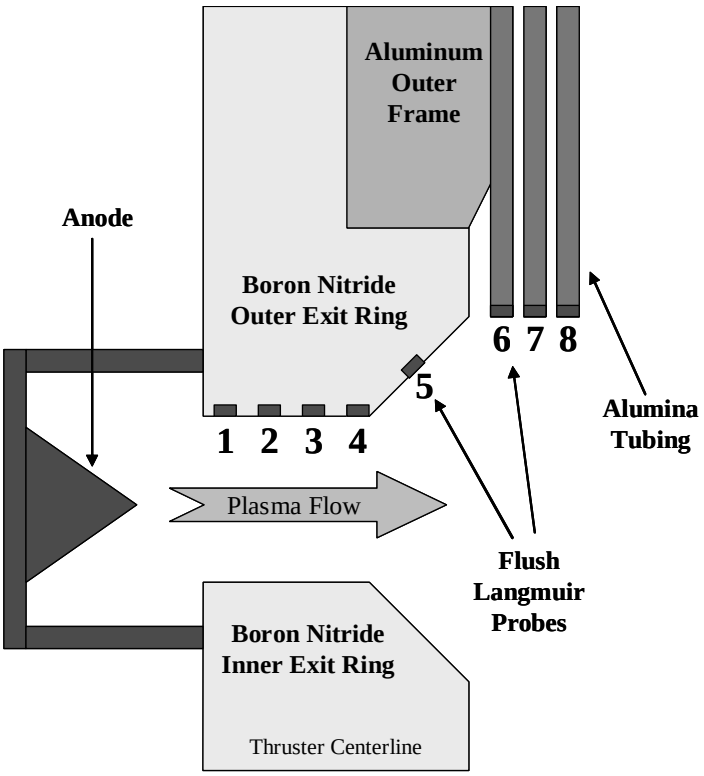

Figure 3.13 Diagram of general axial probe layout and numbering (not to scale).

apart azimuthally, but mounted together on a bracket. Their axial spacing is farther apart and did not warrant azimuthal spacing.

Low Voltage Setup

The low voltage test setup used eight Langmuir probes each with a diameter of 0.020in (0.508mm). Probe data from this setup are reported for discharge voltages between 300-400V. Figure 3.14 shows the axial positions of the probes in relation to the outer exit ring. The axial, radial and azimuthal positions are reported in Table 3.2. As previously mentioned, the interior five probes are spaced apart azimuthally. The azimuthal positions are measured clockwise from the top of the thruster where the cathode is mounted. The radial positions of the probes are measured from the thruster centerline and the axial dimensions are measured from the upstream edge of the outer exit ring. Figure 3.15 shows photographs of the exit ring with the Langmuir probes installed. The lead wires to the probes

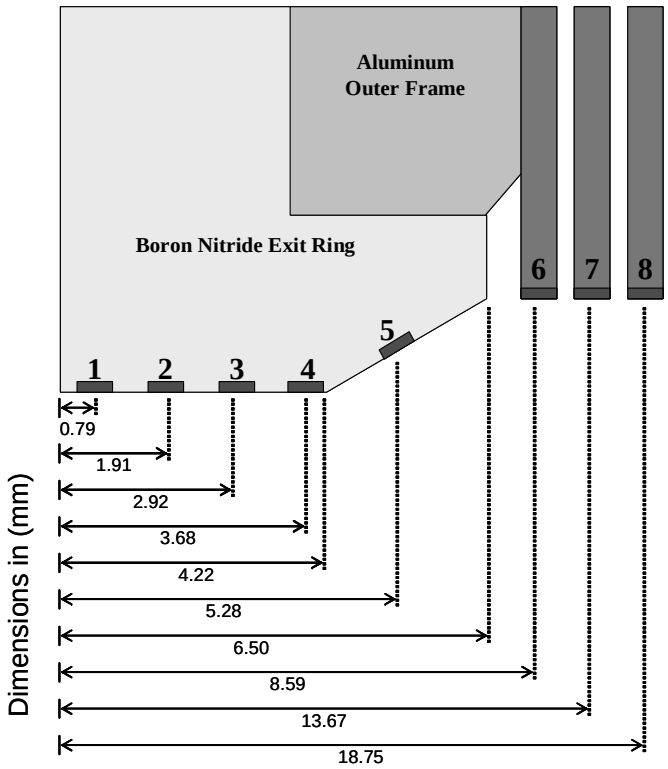

Figure 3.14 Diagram showing axial positions of Langmuir probes in the low voltage test setup. All dimensions in (mm).

TABLE 3.2 Positions of Langmuir Probes in Low Voltage Test Setup

Probe Number	Axial Position (mm)	Radial Position (cm)	Azimuthal Position (degrees)
1	0.79	3.87	81
2	1.91	3.87	75
3	2.92	3.87	69
4	3.68	3.87	63
5	5.28	3.99	106
6	8.59	4.37	90
7	13.67	4.37	90
8	18.75	4.37	90

Figure 3.15 Photographs of the low voltage test setup. Note that there is an extra hole near the chamfer probe that was not used.

were made from a ceramic coated copper wire sometimes used for electromagnets. After looking at the data from the low voltage testing, it was believed that the ceramic insulation suffered very small cracks most likely in places where the wire was bent. These cracks exposed the probe leads to background plasma, causing absorption of leakage currents during operation. The connection between the lead wire and probe was formed with a gold pin, and the entire connection assembly was insulated with high temperature ceramic putty made from aluminum oxide. The putty was hardened using a heat gun and provided structural support to hold the probes in position.

High Voltage Setup

The high voltage test setup used two different probe sizes. Probes 1-5 were made from tungsten wires with 0.015in (0.381mm) diameters. Probes 6-8 were the same size as in the low voltage test with 0.020in (0.508mm) diameters. Probe data from this setup are reported for discharge voltages between 300-900V. Probes 1-5 were reduced in size because probe 4 was collecting too much current at electron saturation for the power supply being used. It was discovered that the 100mA current range of the power supply being

used in the low voltage setup was more of a theoretical limit than a practical limit. At currents near 50mA, the power supply tended to saturate and report only a constant current.

Saturation of the power supply occurred at discharge voltages above 400V, so a new setup was required to perform testing at high voltages. In order to reduce the probe diameter, a new boron nitride outer exit ring was manufactured with smaller probe insert holes. Another problem encountered when pushing the discharge voltage higher was overheating of the external probes. The ion bombardment of the alumina tubing caused the insulation to glow red hot. Therefore, the probes were moved radially outward to reduce the ion heating. The axial dimensions of the high voltage test setup are shown in Figure 3.16 and the full probe positions are reported in Table 3.3. Figure 3.17 contains photographs of the high voltage setup. The lead wires for the high voltage testing were made from triple thick Kapton wire, which proved to be very durable through many hours of testing. The electrical connections between the Kapton lead wires and the probes were made with custom made miniature crimps and insulated with ceramic putty. The putty was dried with a heat gun to provide stiffness and hold the probes in position.

3.4.3 Data Acquisition System

All of the probe leads running from the thruster were ported through the vacuum tank via conducting feedthroughs. Each lead was then wired into a switch box that allowed each probe to be selected individually for operation. The switch box lead was connected to the biasing power supply in order to control the voltage on the selected probe, as well as measure the current collected. The probe power supply was operated, and data were collected, using the LabView software. The low voltage testing used a Keithley 2400 SourceMeter (200V, 100mA) that was biased using an additional power supply in order to operate at higher voltages. The low voltage setup was grounded to the cathode as a reference potential. The high voltage setup used a Keithley 2410 SourceMeter (1100V, 20mA) grounded to the facility. The cathode floating voltage was monitored so that the potential data could be later referenced to the cathode. Both data acquisition setups are shown in Figure 3.18.

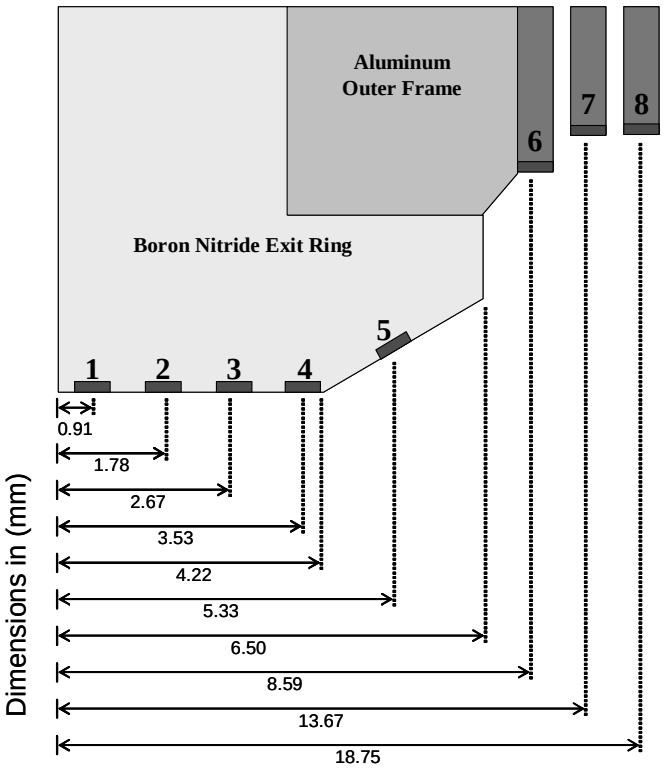

Figure 3.16 Diagram showing axial positions of Langmuir probes in the high voltage test setup. All dimensions in (mm).

TABLE 3.3 Positions of Langmuir Probes in High Voltage Test Setup

Probe Number	Axial Position (mm)	Radial Position (cm)	Azimuthal Position (degrees)
1	0.91	3.87	99
2	1.78	3.87	105
3	2.67	3.87	111
4	3.53	3.87	117
5	5.33	3.98	78
6	8.59	5.08	90
7	13.67	5.40	90
8	18.75	5.40	90

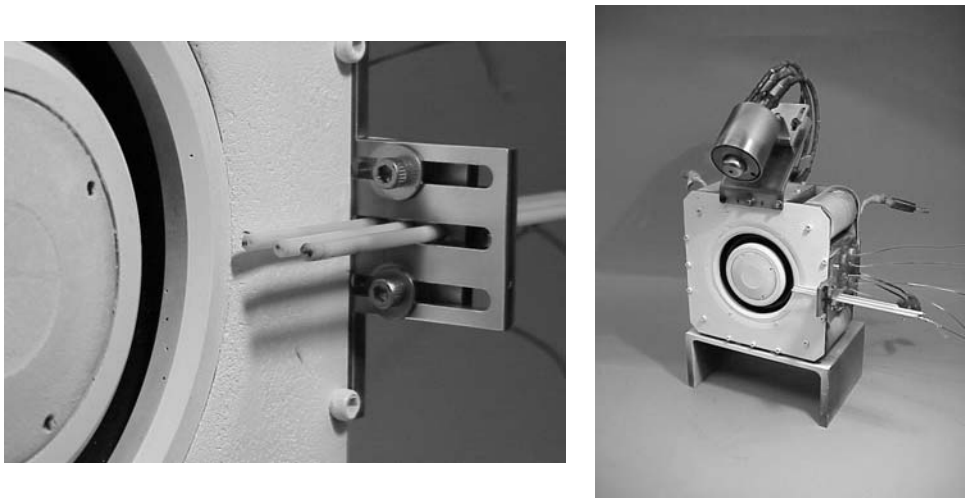

Figure 3.17 Photographs of the high voltage setup. Note the sharp chamfer of the new outer exit ring and smaller internal probe diameters.

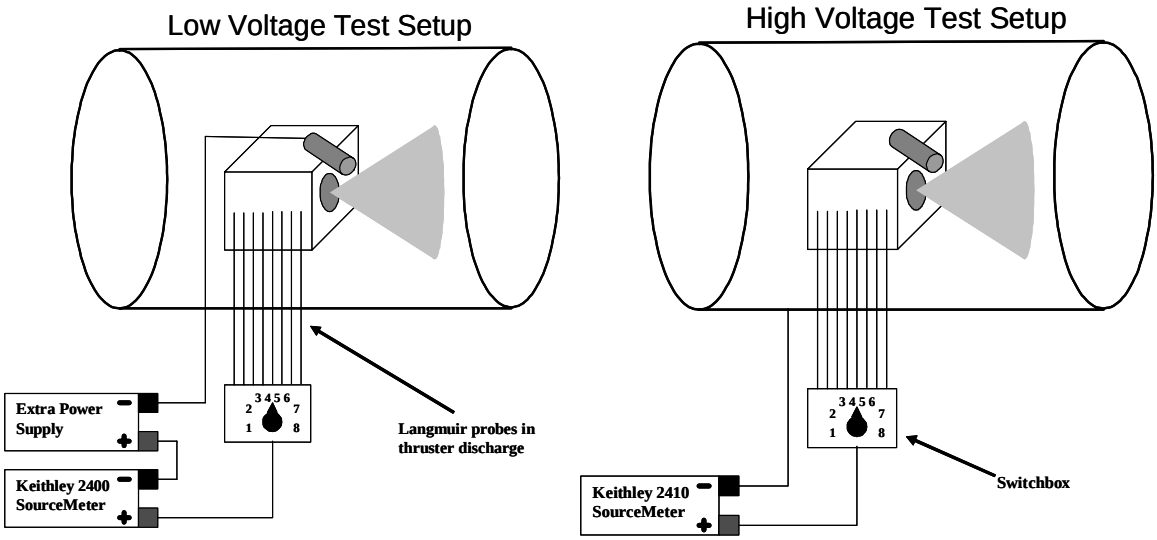

Figure 3.18 Diagram illustrating the two different data acquisition setups. The low voltage setup was grounded to the cathode, while the high voltage setup was grounded to the facility/tank ground. The cathode floating voltage was monitored during the high voltage testing so that both sets of data could be analyzed from cathode potential.

3.5 Langmuir Probe Experimental Results

There were important operational differences between how the low and high voltage tests were performed. Both tests started with a tank pressure near $2x10^{-6}$ Torr before turning the thruster on, and held a pressure in the range of $7x10^{-6}$-$9x10^{-6}$ Torr during operation. Before the low voltage test commenced, the BHT-1000 was allowed to run for over an hour to warm up, allowing the thruster to approach thermal equilibrium as well as to let the thruster materials outgas any moisture absorbed between testing periods. The test began by taking two sets of data at a discharge voltage of 300V, followed by a set of data at 400V, then 500V and finally ending with data at 350V. The thruster operating conditions for the low voltage test are presented in Table 3.4 in chronological order. All of the probe data at each discharge voltage tested was taken starting with the probe furthest upstream and moving in order downstream, except at 500V. The 500V data is not reported here because the internal probes were drawing too much current for the power supply to operate properly and the external probes were overheating at times. The first set of 300V data is also not reported, as the magnetic field settings did not match those of the other data. The magnet currents were not tuned continuously during probe measurements as they were during the performance testing.

TABLE 3.4 Low Voltage Test Conditions

Start Time[1]	Φ_d (V)	I_d (A)	I_{inner} (A)	I_{outer} (A)	$\dot{m}_a$ (mg/s)	$\dot{m}_c$ (mg/s)
3:09PM	300	2.07	8.0	8.0	2.5	0.30
3:54PM	300	2.06	11.1	8.0	2.5	0.30
4:22PM	400	2.01	11.1	8.0	2.5	0.30
5:11PM	500	2.08	11.1	8.0	2.5	0.30
6:42PM	350	2.03	11.1	8.0	2.5	0.30

1. Thruster was started at approximately 2:00PM.

The low voltage test data were previously published [20] but have been reanalyzed since then, with minor improvements made to the data analysis technique. The high voltage test procedure was organized with more structure after research at the NASA Glenn Research

Center showed that the acceleration layer in the discharge plasma moves axially inward as the discharge voltage is increased [19]. When this high temperature and density region moves inward towards the anode, it can burn off deposited materials on the ceramic exit ring, changing the plasma properties. It was therefore decided that the high voltage test should be performed in descending order of discharge voltage, allowing all ceramic erosion and outgasing to occur before data were taken. Therefore, the high voltage test began by letting the thruster warm up for an hour and thirty minutes at 300V and then another two hours at 900V before data collection started. The order of data collection and thruster conditions are presented in Table 3.5. All of the probe data at each discharge voltage were taken starting with the probe furthest upstream and moving in number order downstream.

TABLE 3.5 High Voltage Test Conditions

Start Time[1]	Φ_d (V)	I_d (A)	I_{inner} (A)	I_{outer} (A)	$\dot{m}_a$ (mg/s)	$\dot{m}_c$ (mg/s)
5:45PM	900	2.23	11.1	8	2.5	0.25
6:36PM	750	2.21	11.1	8	2.5	0.25
7:09PM	600	2.18	11.1	8	2.5	0.25
7:33PM	450	2.15	11.1	8	2.5	0.25
7:56PM	300	2.08	11.1	8	2.5	0.25

1. Thruster was started at 2:15PM.

3.5.1 Low Voltage Results

Figure 3.19 shows an axial profile of electron temperature. All of the low voltage test results are plotted with the axial position measured from the upstream edge of the outer exit ring, as shown in Figure 3.14. The plot shows that the peak electron temperature occurs near probe 5 on the chamfer and increases with discharge voltage. This peak temperature is generally where the electrons have reached their maximum kinetic energy as they accelerate towards the anode. It signals the start of the ionization layer from an electron point of view as it travels upstream. Although it is difficult to be sure, it looks as if the peak temperature region may be moving upstream as the discharge voltage increases, particularly in the increase from 300V to 350V. At the probes furthest upstream, the elec-

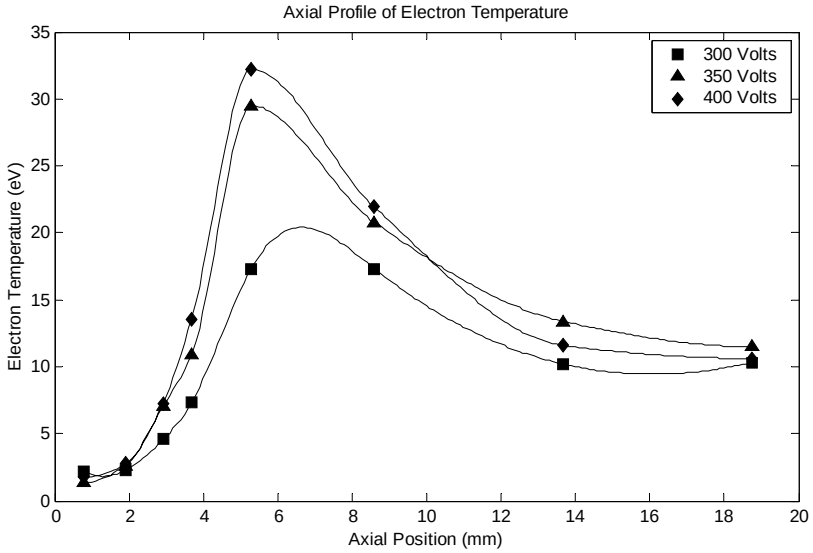

Figure 3.19 Axial profiles of electron temperature for various discharge voltages tested with the low voltage setup.

tron temperature is nearly constant with discharge voltage. Probes 1 and 2 measured approximately 3eV or less for all three discharge voltages reported. This near anode region likely does not participate in the ionization, as the electron energies are small here, indicating their potential for ionizing collisions is low.

The axial profile of plasma potential is shown in Figure 3.20. It can be seen from the figure that the plasma potential inside the discharge channel is nearly constant and approximately equal to the anode potential. The decrease in potential beginning between probes 4 and 5 indicates the start of the acceleration layer for ions moving downstream. The plot of floating potential displayed in Figure 3.21 looks very similar to the plasma potential profile. The floating potential drops off sharply between probes 4 and 5, and is nearly constant in the external probes.

The axial profile of electron density is pictured in Figure 3.22. The peak densities measured for all three voltages occurred at probe 4, and were of the same order of magnitude. The sharp drop in density at probe 5 could be a wake effect occurring because the chamfer probe sits around a corner from the main discharge (see Figure 3.13). The ions streaming

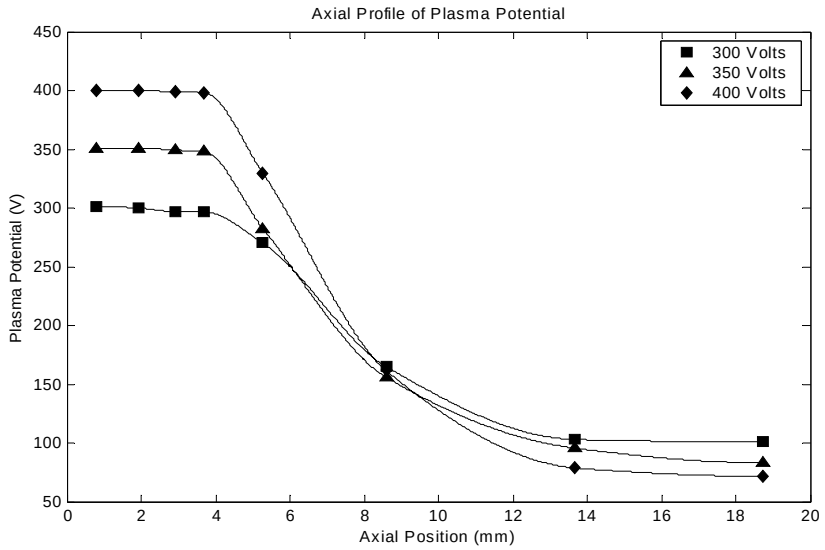

Figure 3.20 Axial profiles of plasma potential for various discharge voltages tested with the low voltage setup.

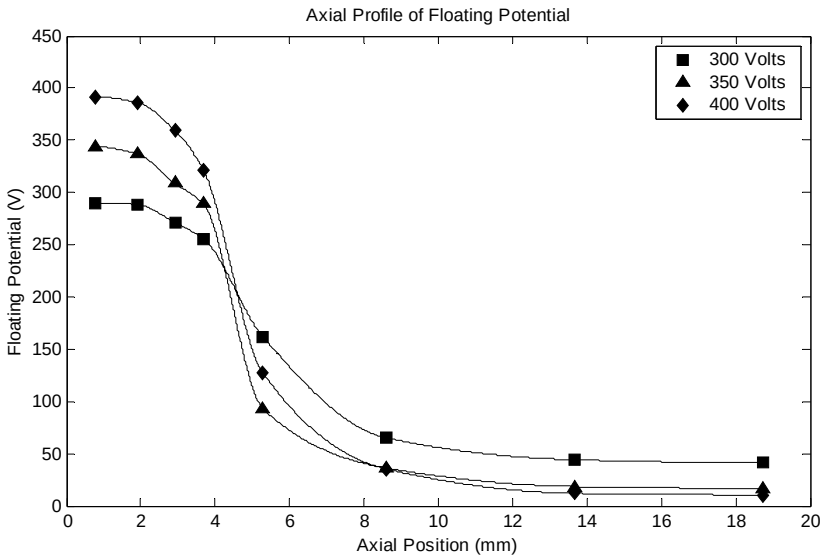

Figure 3.21 Axial profiles of probe floating potential for various discharge voltages tested with the low voltage setup.

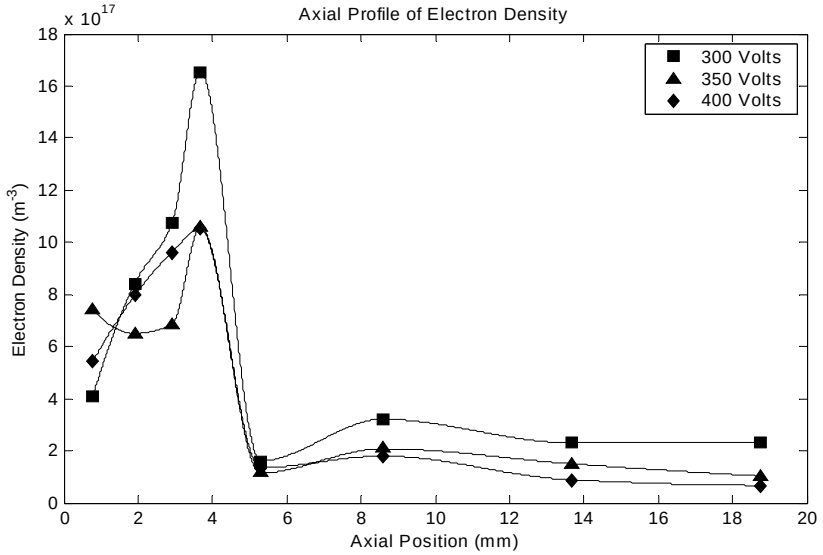

Figure 3.22 Axial profiles of electron number density for various discharge voltages tested with the low voltage setup.

out of the discharge chamber with high axial velocity may not turn the chamfer corner sharply enough to reach probe 5, thus preventing electrons from arriving as well because of quasineutrality. This issue will be discussed further in the following chapter.

3.5.2 High Voltage Results

All of the high voltage test results are plotted with the axial position measured from the upstream edge of the outer exit ring, as shown in Figure 3.16. The axial profiles of electron temperature are plotted in Figure 3.23 for all five voltages tested. As in the low voltage test results, the peak temperature measured occurred at probe 5 on the chamfer, with the exception of the 450V data. The temperature at probe 5 (as well as several other probes) looks to rise almost linearly with discharge voltage. It is difficult to determine where the true peak electron temperature occurs. The relatively high temperatures measured at probe 4 for discharge voltages above 300V seem to indicate that the maximum temperature may occur somewhere between probes 4 and 5. Despite this, it is easy to see that discharge voltage has a very strong effect on the peak electron temperature. The temperatures measured far upstream are relatively unaffected by discharge voltage, as was the

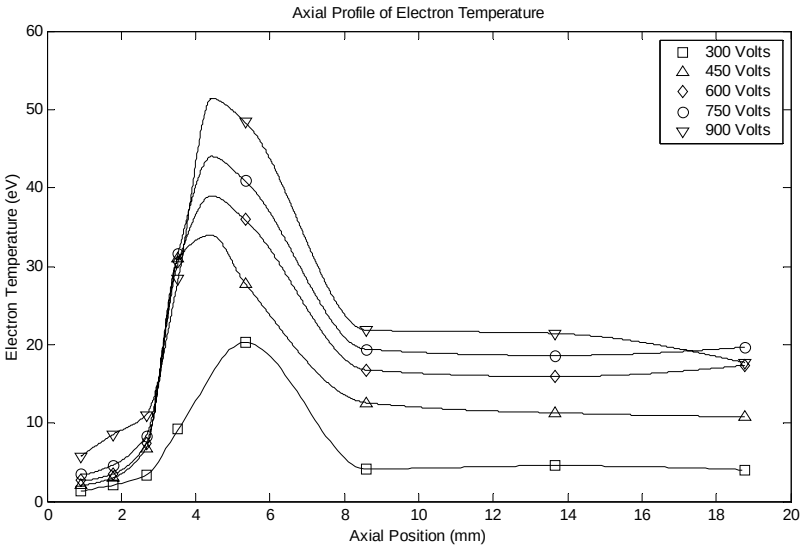

Figure 3.23 Axial profiles of electron temperature for various discharge voltages tested with the high voltage setup.

case in the low voltage testing. The external probes seem to show a fairly linear increase of electron temperature with voltage. The relationship between temperature and discharge voltage will be explored further in the following chapter.

Figure 3.24 shows the axial profiles of plasma potential measured for each discharge voltage tested in the high voltage configuration. As with the low voltage testing, the four probes furthest upstream show a nearly constant plasma potential with magnitudes nearly equal to the discharge potential. Some of the profiles show very slight increases in potential before the ion acceleration layer begins between probes 4 and 5. As the discharge voltage is increased, it was observed that the plasma potential on the interior probes drops slightly relative to the discharge potential. The potentials measured at the exterior probes were nearly constant and low. Figure 3.25 shows the profiles of floating potential measured by the probes. The profiles are similar in shape to the plasma potential profiles, as was the case with the low voltage testing. The decrease in potential begins a bit further upstream (between probes 3 and 4), corresponding to the measured increase in electron temperature in the same region. Some of the floating potentials measured at the exterior

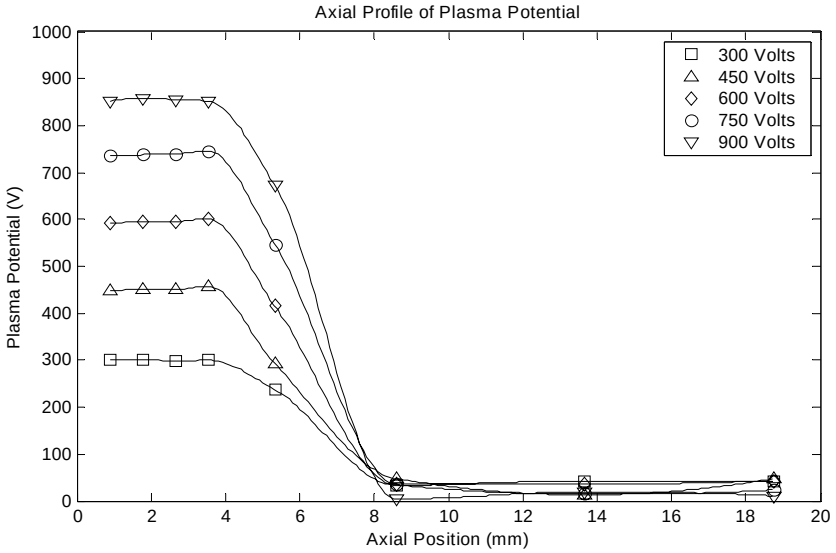

Figure 3.24 Axial profiles of plasma potential for various discharge voltages tested with the high voltage setup.

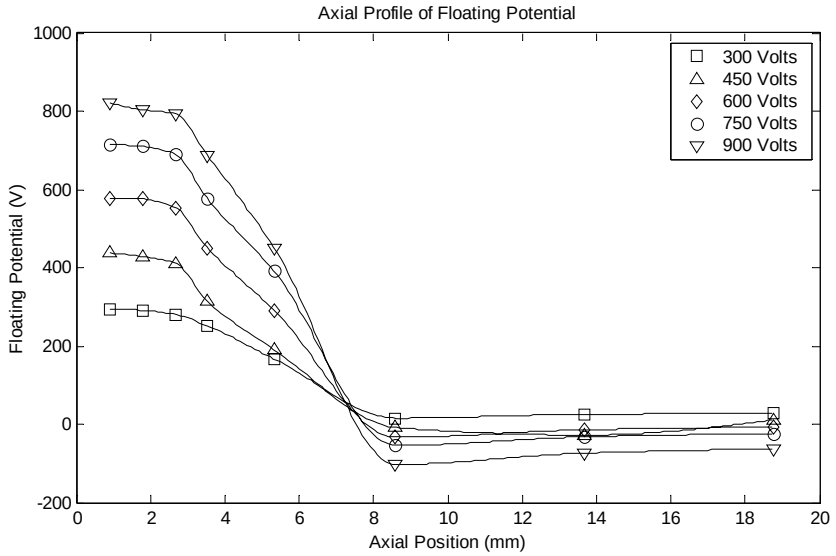

Figure 3.25 Axial profiles of probe floating potential for various discharge voltages tested with the high voltage setup.

probes were actually negative relative to the cathode, likely due to their positions. Because these probes were placed far out radially in order to avoid overheating, this region was likely out of the main plume expansion and devoid of ions, thereby reducing the potential.

Figure 3.26 presents the axial profiles of electron number density for each voltage tested. The peak densities measured are nearly equal for each of the voltages, but the shapes of the profiles in the upstream region vary. The 300V curve shows a very smooth increase towards a peak density at probe 4, whereas the other profiles show sharper increases near the peak density. All of the profiles show a peak density at probe 3, with the exception of the 300V and 900V data, which peak at probe 4. The exterior probes all measured relatively low densities. The wake effect observed in the low voltage setup was less obvious in the high voltage testing, most likely because probes 6-8 were positioned further out radially and may also have experienced wake effects similar to those seen at probe 5. Thus, all four of the probes furthest downstream measured very low densities due to wake effects, making the effect at probe 5 more difficult to see in the axial profile.

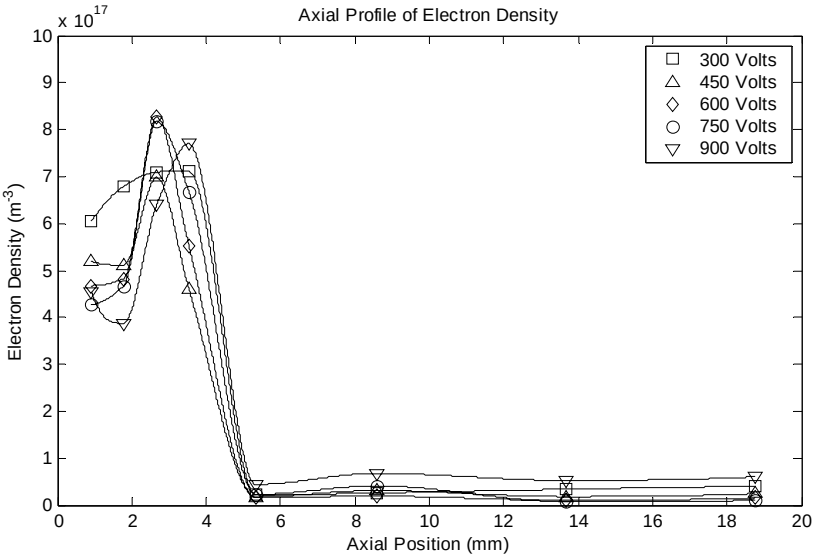

Figure 3.26 Axial profiles of electron number density for various discharge voltages tested with the high voltage setup.

Chapter 4

ANALYSIS AND DISCUSSION OF RESULTS

4.1 Performance Testing of the BHT-1000

The performance of the BHT-1000 Hall thruster must be evaluated in the context of the thruster's objectives. It was designed as a high specific impulse thruster to fill the need previously outlined by NASA for an efficient means of stationkeeping and interplanetary orbit transfer within the solar system. The BHT-1000 is already considered to be a thruster pushing the specific impulse operational envelope of current Hall thruster technology [21]. The results of performance testing completed in this research did not show significant improvements over that of previous research [8]. The goal was simply to match previous performance and record a baseline set of performance data for analysis.

During the performance testing detailed in Chapter 2, the BHT-1000 was able to demonstrate almost 3100s of specific impulse and produce over 90mN of thrust while operating at a discharge power of just over 2600W. This type of performance puts the BHT-1000 at the forefront of Hall thruster technology, and slightly closer to the original design goals of 3000s of specific impulse and 100mN of thrust at a power of 2300W. When using the two stage configuration, slight increases in specific impulse and thrust were demonstrated at the discharge voltages tested in this research. Increases in thrust efficiency were also shown at some voltages. The discharge power also increased, possibly due to increased ionization, as the ionization layer is established between the anode and intermediate electrode. However, if improvements are made to the placement and size of the intermediate

electrode, the two stage technology may be used to provide a significant performance improvement over single stage operation.

The single stage performance can be compared to results of the full PIC simulation used at Busek. The simulation is described in more detail in the following section. The predicted and actual performance numbers are displayed in Table 4.1 for an anode flow rate of 2.5 mg/s. Several trends are apparent in the comparison. The simulation tends to underpredict the discharge current and therefore the discharge power as well. Thrust is also underpredicted by the simulation, an effect related to the low discharge current. The simulation tends to run with lower utilization than the estimates of utilization made during performance testing. This lower utilization means that less ionization occurs in the simulation, and thus lower electron current is received at the anode. Fewer ions are produced for the same reason, and thus thrust is underpredicted. Specific impulse matches well at 300V, but is far underpredicted by the simulation at the higher voltages. Conversely, the efficiency numbers match better at the higher voltages, with the main discrepancy occurring at 300V.

TABLE 4.1 Comparison of Experimental and Simulated Performance of the BHT-1000 at $\dot{m}_a$ =2.5 mg/s

Condition	**Simulation Results**			**Experimental Results**		
Φ_d (V)	300	600	900	300	600	900
I_d (A)	1.50	1.63	1.68	1.96	2.07	2.18
T (mN)	34.8	50.3	61.1	35.2	55.5	70
I_{sp} (s)	1420	2050	2493	1472	2264	2853
η	0.54	0.53	0.52	0.43	0.50	0.50

4.2 Comparison of Probe Results to PIC Code Predictions

As discussed in the research objectives outlined in Chapter 1, the main thrust of this research was to provide internal plasma property data for comparison to and validation of the PIC simulation being developed at the Busek Co. A short description of the code is provided, as well as some explanation of the methods used for making comparisons

between the probe data and the PIC code results. Also, some possible explanations for discrepancies between the measured and simulated plasma properties are discussed.

4.2.1 Two Dimensional PIC Simulation Description

The two dimensional simulation is fully kinetic and uses Particle-in-Cell (PIC) and Monte Carlo Collision (MCC) methodologies. The numerical model includes electrons, neutrals, singly and doubly charged ions, as well as a realistic thruster geometry that includes dielectric walls and secondary electron emission. The electric potential is calculated by solving a form of Poisson's equation. Ion-electron recombination is modeled at dielectric boundaries and neutrals are recycled. The sheath is calculated by collecting the residual charges and incorporating them into the potential calculation. The simulations described here include elastic and inelastic (excitation, ionization) electron-neutral collisions, electron-ion ionizing collisions, ion-neutral scattering, and charge exchange collisions. By using an artificial mass ratio and artificial permittivity, the full PIC code is able to capture oscillations on the scale of the electron plasma frequency. Anomalous diffusion is included via an equivalent scattering frequency where the Hall parameter can be stipulated. Typical runs of the code take several days. The model was originally developed by Szabo at MIT and has been well described in previous publications [6, 22].

The most significant recent change to the code is a revised ion accommodation coefficient at solid surfaces. As before, full accommodation of ion momentum (diffuse reflection) is assumed and partial accommodation in energy. However, previous simulations assumed a recycled neutral retained 50 percent of its parent ion's kinetic energy. Current simulations assume an energy accommodation coefficient of α=60 percent at energies less than 140eV, α=77 percent at energies greater than 400eV, and a linear fit between the endpoints at energies in between. These values are based upon experimental measurements of xenon accommodation on boron nitride by RIAME and MAI [23].

The 2-D simulation was run with the as built BHT-1000 geometry and a magnetic field generated by the Maxwell software package. Simulations at a particular discharge poten-

tial may be compared directly to probe data taken at the same discharge potential. An artificial mass ratio of 2500 was assumed, which means that m_i/m_e~96. Various scaling factors were used to produce physical results. Stochastic Bohm type diffusion was added with a proportionality coefficient of 1/200, as opposed to the classical value of 1/16, meaning that the anomalous Hall parameter is 200. Free space permittivity is typically increased by a factor of 400, which lengthens the Debye length by a factor of 20. Thus, a coarser grid can be used, and the plasma frequency decreases by the same factor, allowing for a longer time-step. The run time on an AMD Athlon powered PC for a single case with m_i/m_e~96 is several days.

4.2.2 Comparison Methodology

It is unclear what physical region of the discharge plasma each Langmuir probe samples, and it is therefore also difficult to determine what simulation data should be used for comparison to experimental results. In an infinite, quiescent plasma, the probes would sample the far away region of constant potential and electron density. Thus, in this first cut comparison, the simulated data along the thruster centerline (which is the radial point furthest from both channel walls) was considered to be the probe sampling region. Contour maps of the plasma parameters as calculated by the simulation are presented in Figure 4.1. Also pictured in each of the plots are the magnetic streamlines that intersect each of the eight Langmuir probes tested in the low voltage configuration (bowed vertical lines). It is easy to see that these magnetic field lines have a curved shape. Because electrons are free to move along these magnetic field lines, their shape must be considered. Therefore, when comparing the probe results to the predicted plasma parameters along the thruster centerline, one must compare to the plasma parameters at the intersection of the streamline originating from the appropriate probe with the thruster centerline. It is recognized that this is only a first approximation and a finer simulation of the near probe region would be required for a more rigorous comparison.

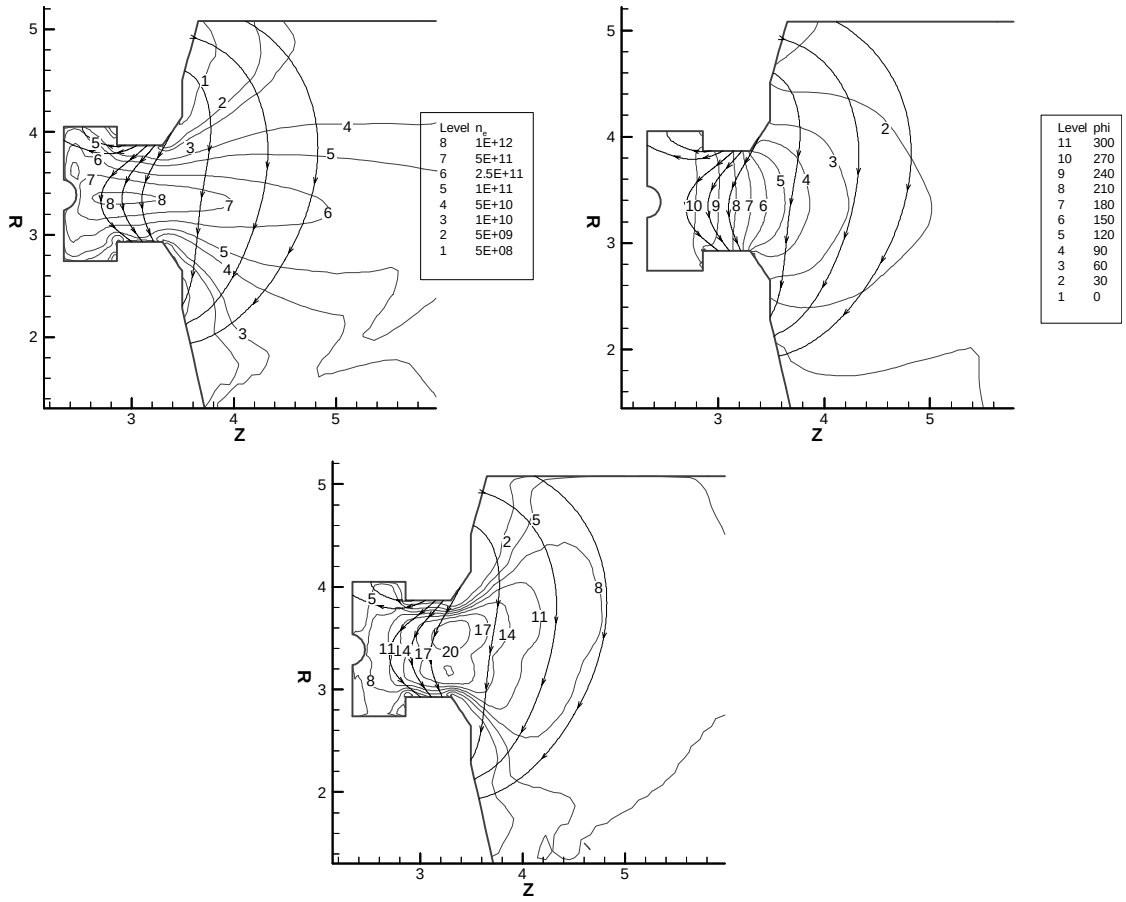

Figure 4.1 Contour plots of plasma parameters as determined the by the 2-D full PIC simulation at a discharge voltage of 300V. The bowed vertical lines are the magnetic streamlines that intersect each of the eight Langmuir probes tested in low voltage configuration. Top left: contour plot of electron density. Top right: contour plot of electric potential. Bottom: contour plot of electron temperature.

In making comparisons of the axial profiles of plasma properties, the full PIC data were interpolated to a line at a radius of R=3.4cm, the centerline of the thruster channel. The probe data were plotted at axial positions that correspond to the axial position of where their respective magnetic streamlines intersect the thruster centerline. Note that the probe positions are now in the simulation coordinates, instead of being measured from the upstream edge of the outer exit ring. These coordinates are illustrated in Figure 4.1 with the axial zero position placed at the base of the anode cone and the radial zero position being on the centerline axis of the thruster. For example, probe number 3 in the low volt-

age setup is located physically at Z=3.15cm, but the magnetic streamline intersecting that probe crosses the centerline (R=3.4cm) at Z=2.71cm. Thus, the data point for probe 3 is plotted at Z=2.71cm. The magnetic streamlines that intersect probes 1-2, the probes furthest upstream in the thruster, do not intersect the thruster centerline, which was the case in both the low and high voltage configurations. They are therefore not plotted in the comparison of probe results to the code predictions along the channel centerline.

The actual probe positions along with the centerline positions followed from their intersecting magnetic streamlines are shown in Table 4.2. The positions are given in centimeters in the simulation coordinate system.

TABLE 4.2 Positions Used for Comparison of Probe Data to Simulation Data

Probe	Low Voltage Axial Position[1]	Low Voltage Centerline Axial Position	High Voltage Axial Position	High Voltage Centerline Axial Position
3	3.15	2.71	3.12	2.62
4	3.23	2.91	3.21	2.88
5	3.39	3.11	3.39	3.13
6	3.72	3.69	3.72	4.58
7	4.22	4.29	4.22	5.25
8	4.73	4.77	4.73	5.56

1. All positions in this table are in simulation coordinates and listed in centimeters.

4.2.3 Low Voltage Comparison Results

The probe data from both the low and high voltage test setups were compared to simulation results. For the low voltage data, the probe data taken with discharge potentials of 300V and 400V were compared to simulation predictions for the same voltages. The axial profiles of electron temperature, plasma potential and electron density can be found below. As previously mentioned, probes 1 and 2 are not included in this comparison. The probes compared are probes 3-8, numbering in the downstream direction as in Chapter 3.

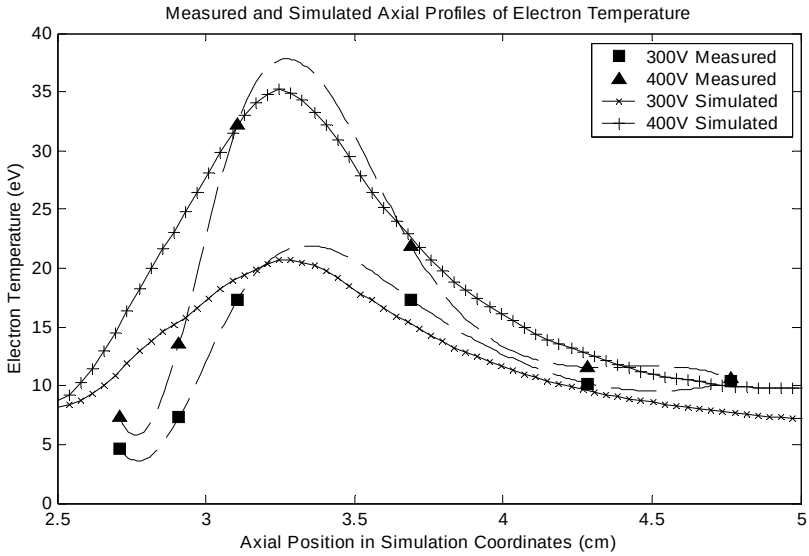

Figure 4.2 Comparison of electron temperature results from the low voltage test setup with predictions from the PIC simulation.

The low voltage comparison of electron temperature in Figure 4.2 shows good agreement between the experimental results and the simulation. Electron temperatures are very close to agreement in probes 5-8 and not far from agreement in probes 3-4. The trend of having a peak electron temperature between probes 5 and 6 is reflected in the code results and can be visually interpolated to fit well with the experimental results. However, the initial rise in electron temperature measured from probes 3-5 seems to happen over a shorter axial distance than in the simulation.

The comparison of measured plasma potential in the low voltage configuration to PIC results pictured in Figure 4.3 shows very good agreement. The simulation seems to start a more gradual decrease in potential further upstream than the experimental results reflect, but the trends match well.

The profiles of electron density in Figure 4.4 do not agree as well as the other plasma properties. The peak density for the 300V experimental data is nearly 50 percent higher than the peak density calculated by the simulation. The peak density measured for a discharge voltage of 400V matched well with the simulation, but both voltages showed

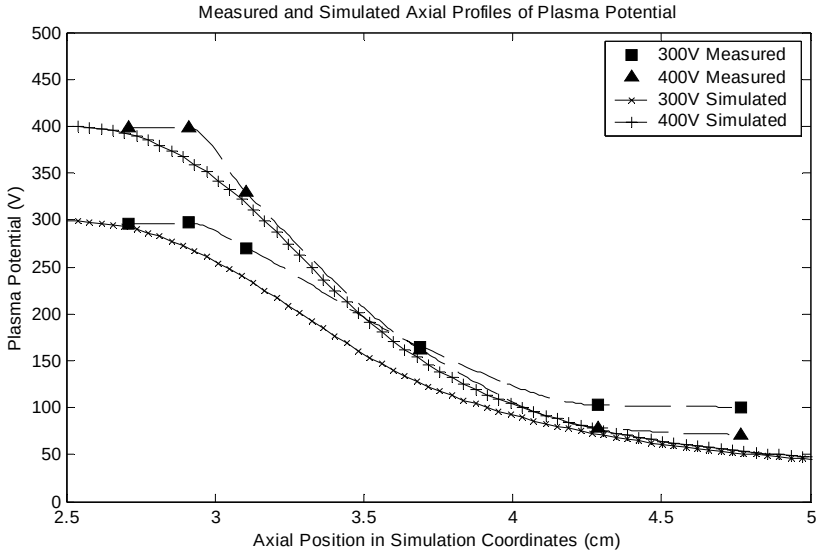

Figure 4.3 Comparison of plasma potential results from the low voltage test setup with predictions from the PIC simulation.

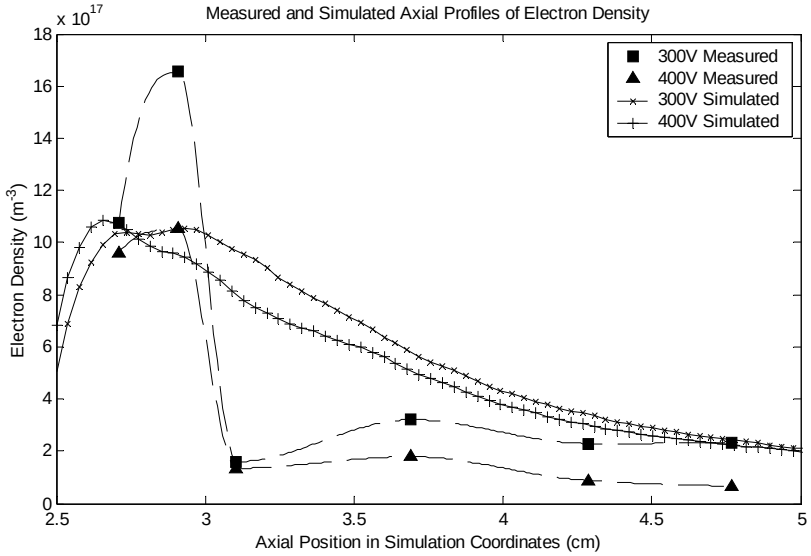

Figure 4.4 Comparison of electron density results from the low voltage test setup with predictions from the PIC simulation.

drastically different overall trends in density. The drop in density measured is much sharper than in the simulation, especially in the region between probes 4 and 5. The low density measured at probe 5 may actually occur because of a wake effect, as previously mentioned in Chapter 3.

A relatively simple calculation based on a Prandtl-Meyer expansion fan emanating from the sharp convex corner on the outer exit ring, where the chamfer begins, can help illustrate the wake effect mechanism. The turning angle of the flow (equal to the angle of the chamfer) is about 50 degrees. If the incoming flow is assumed the be sonic, then the decrease in density can be as great as an order of magnitude, depending on the ratio of specific heats, γ. If γ=1.4 or even if γ=5/3, the decrease in density is approximately an order of magnitude. If γ is only unity, the decrease in density around the chamfer is still greater than 50 percent. This type of wake effect can have a strong influence on the measured density near thruster surfaces.

4.2.4 High Voltage Comparison Results

For the high voltage comparison, the probe data taken with discharge potentials of 300V, 600V and 900V were compared to simulation predictions for the same voltages. The axial profiles of electron temperature, plasma potential and electron density can be found below. The plot of electron temperature shown in Figure 4.5 shows better agreement at the lower voltages than the higher voltages. As in the low voltage comparison, the axial spread is larger in the PIC data, with the probe data rising more sharply to peak temperature. There is a large axial distance of unprobed area between probes 5-6 because of the shape of the magnetic streamlines near probe 6. This probe was placed at a larger radial position in the high voltage setup and thus its intersecting magnetic streamline bowed out farther axially at centerline.

The agreement in plasma potential shown in Figure 4.6 is very good in the region of probes 3-5. The exterior probes match well at 300V, but not quite as well at the higher voltages. Again, the probes measured a sharper profile of the acceleration region where

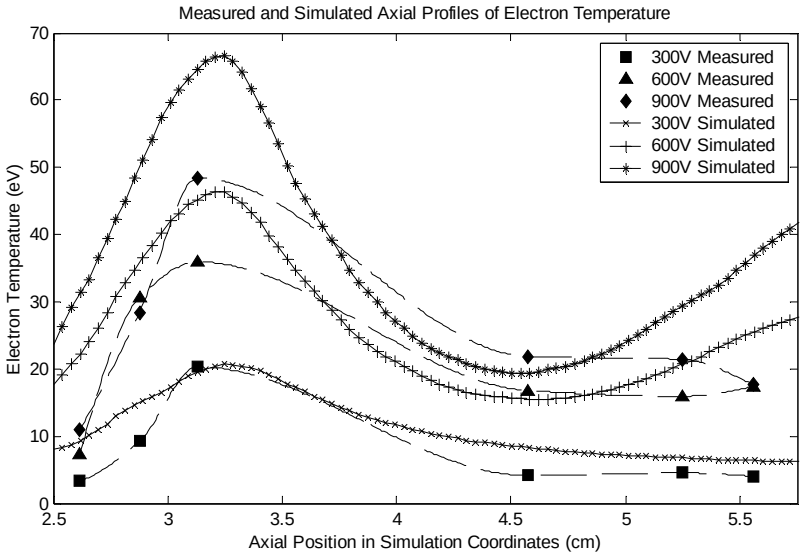

Figure 4.5 Comparison of electron temperature results from the high voltage test setup with predictions from the PIC simulation.

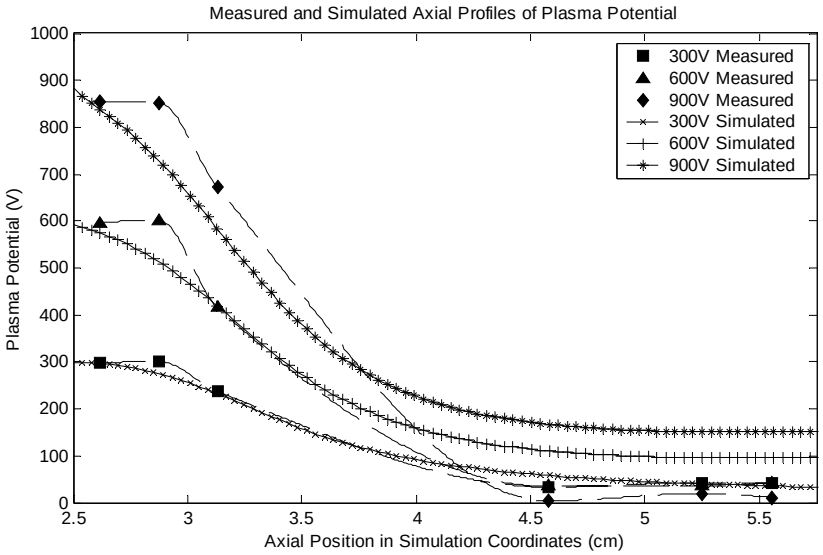

Figure 4.6 Comparison of plasma potential results from the high voltage test setup with predictions from the PIC simulation.

the potential falls quickly in the axial direction. The PIC simulations show a more gradual decrease in plasma potential that begins further upstream, spreading the width of the acceleration region.

As with the low voltage comparison, the high voltage data of electron density shown in Figure 4.7 only matches qualitatively near the internal probes. Probe 5 exhibits the wake effect discussed earlier and the exterior probes demonstrate very little change in density in the axial direction. The peak densities measured at 600V and 900V correlate well to the peak densities calculated by the simulation, but the 300V peak density does not match as well. The axial spreading of plasma parameters shows up again in this plot of electron density, with the PIC predictions seemingly smearing the plasma discharge over a wider axial distance than the probes measured.

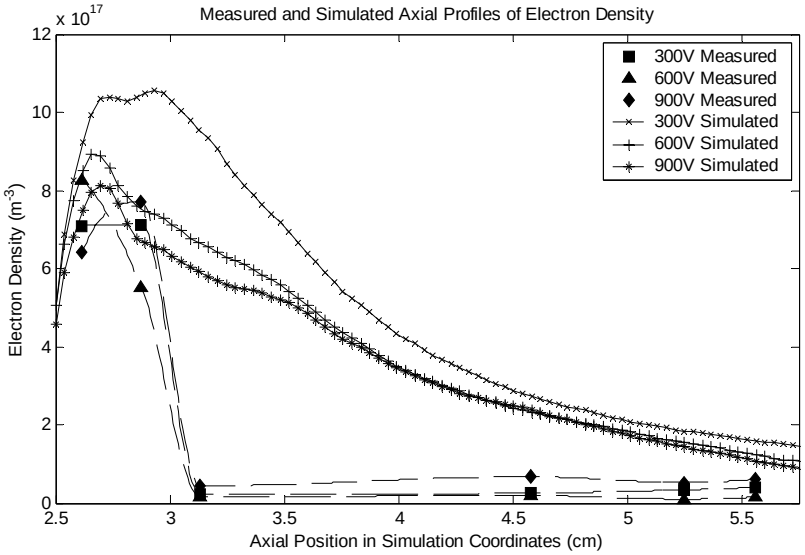

Figure 4.7 Comparison of electron density results from the high voltage test setup with predictions from the PIC simulation.

4.2.5 Comparison Discussion

Another effect that may help to explain the discrepancies in electron density is the intersection angle of the magnetic streamlines. To arrive at an estimate of electron density, the electron saturation current was determined and then the full physical probe area was used to estimate the flux of electrons. However, the electrons are strongly contained by the magnetic field. Given the electron temperatures measured and assuming the electron velocity is determined by temperature alone, the Larmor radius (the radius at which electrons gyrate about magnetic field lines) for a single electron can be determined from,

$$R_{Larmor} = \frac{m_e v_e}{eB}. \tag{4.1}$$

At the low voltage configuration probe positions, the Larmor radius varies between approximately 0.1-0.4mm. The probe diameter in the low voltage setup is 0.508mm and therefore, the Larmor radius is comparable to the probe radius and indicates that the magnetic field may play an important role in the trajectory of the electrons.

When the magnetic field lines intersect the probe surfaces at an angle and the Larmor gyrations are tight enough, the stream tube's effective area may be decreased. If the electrons are considered as flowing through a tube that ends at an angle, then the cross section of the tube determines the flux to the probe. The effective area would then be,

$$A_e = A_p \cos(\theta), \tag{4.2}$$

where θ is the angle of the intersecting magnetic streamline to the normal of the surface, as illustrated in Figure 4.8. This angle factor can be significant. The magnetic streamlines shown in Figure 4.1 intersect the walls at the angles estimated in Table 4.3. These angles are for the probes in the low voltage test setup. The largest angle is at the probe located on the chamfer, where the largest difference between the simulation and the probe measurements was observed. Figure 4.9 shows the effect this factor can have on the axial profile of density and its comparison to the simulation in the low voltage case. The full correction

shown corresponds to the limit where $R_{Larmor} << R_{probe}$. Since these radii are actually comparable, the true correction should probably be intermediate. The correction does seem to smooth out the density profiles and reduce the wake effect of the chamfer on probe 5. However, even though the density measured at probe 5 matches the simulation better with the correction, the probes further upstream seem to match worse with the stream tube correction. This effect is obviously not the only error, but it may be important.

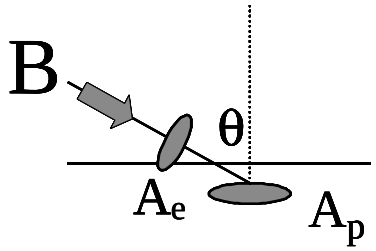

Figure 4.8 Illustration supporting the magnetic stream tube angle argument. The effective area of the probe is decreased because the field line intersects the probe at an angle.

TABLE 4.3 Angle of Intersection of Magnetic Field Lines with Probes in the Low Voltage Test Setup

Probe	Angle (degrees)
1	73
2	59
3	47
4	40
5	76
6	18
7	21
8	19

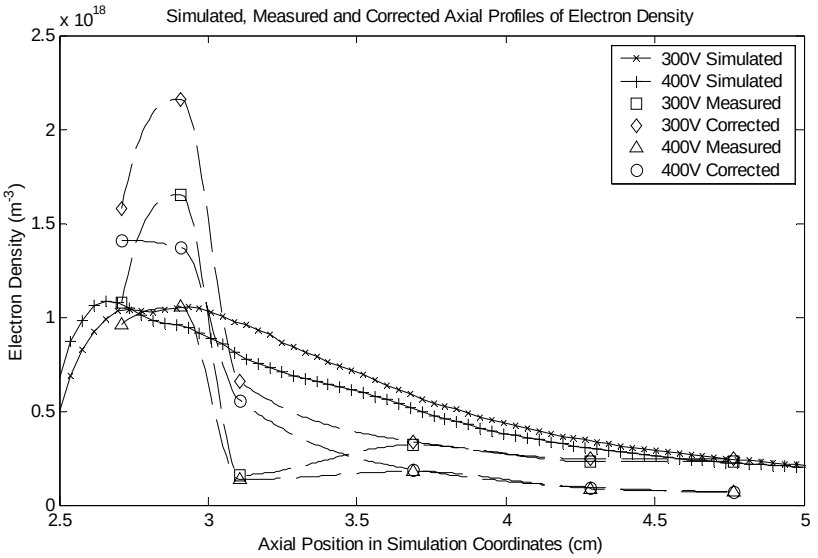

Figure 4.9 Axial profiles of electron density from the low voltage setup illustrating the magnetic stream tube correction for angled magnetic streamlines.

An important consideration in comparing the probe measurements to the simulation results is the determination of the actual sampling region of the probes. For a Langmuir probe sitting behind a plasma sheath and pre-sheath, but in contact with an infinite plasma, the probe samples the plasma parameters (n_e, V_p, T_e) in the far away region. However, in the relatively small discharge channel where the pre-sheaths from either side of the channel may in fact connect with each other, it is difficult to determine what plasma the wall probes are sampling. In this work, the assumption was made that the probe "sees" the peak (centerline) potential, density and temperature along the local magnetic field line. More analysis and modeling will be necessary to confidently resolve this important question.

The axial plasma parameter plots comparing the simulation to the experimental data suggest that the simulation is actually smearing the plasma over too wide of an axial region. The measured electron densities tend to fall off much more sharply than the simulation predicts, while the electron temperatures tend to rise more sharply than predicted. Furthermore, the predicted plasma potential tends to decrease constantly from the anode,

while the measured plasma potential along the internal discharge chamber remains relatively constant until the chamfer begins. This smearing of the main discharge is suggested by other data presented elsewhere as well. Ionization frequency measurements of the BHT-1000 and their comparison to the 2-D full PIC simulation have been published previously and also suggest this same widening effect in the code [24]. This effect has also been seen in the modeling of the Michigan P5 thruster being done at MIT. A comparison of full PIC results for the P5 thruster with experimental data suggests that the main discharge is much more axially confined than the code predicts. In the 1-D modeling done by Ahedo, this smearing effect has been observed as well [26].

The widening of the discharge in simulations could be due to several effects. Too much electron diffusivity may be a potential explanation. Computations using a classical anomalous Hall parameter of 16, or even 64, tend to diverge. The full PIC computations taking place at MIT and Busek use anomalous Hall parameters closer to 200 (BHT-1000 thruster) or even 400 (Michigan P5 thruster) in order to find a best fit of modeling results to reality. A different explanation for the widening of the computed plasma profiles could be the existence of unmodeled ionization enhancing mechanisms. The current PIC codes use an ionization rate expression derived from the assumption of direct ionization by electron impact from the atom's ground state. If a meta-stable state were present, it might be populated enough to allow even low energy electrons to ionize from it. Similar effects might arise from trapping of ultraviolet radiation, which might over populate some upper excited levels.

4.3 Peak Electron Temperature Analysis

The region of peak electron temperature occurred closest to probe 5 for most of the discharge voltages tested. The dependence of the peak electron temperature on discharge voltage is less than proportional, as shown in Figure 4.10. The measured plot is taken from probe 5 in the high voltage setup, while the simulated data are taken as the peak elec-

tron temperature calculated in the near exit plane region. Both the experimental and the simulation data were fitted with power laws of the form,

$$T_e = a\Phi_d^{\,n}, \tag{4.3}$$

where *a* and *n* are both constants and the electron temperature is in units of electronvolts. The constants were determined by anchoring the fit to the end points of the data, which are at 300V and 900V for both the experimental and simulation data. The equation for each fit is shown in Figure 4.10. It is easy to see that, unlike the experimental data, the simulated electron temperature actually begins to rise faster as discharge voltage is increased. Most of the probes used in the high voltage setup showed a near linear (but not proportional) dependence of electron temperature on discharge voltage, except at probe 4. This probe was found to have an almost constant electron temperature for all discharge voltages tested above 300V.

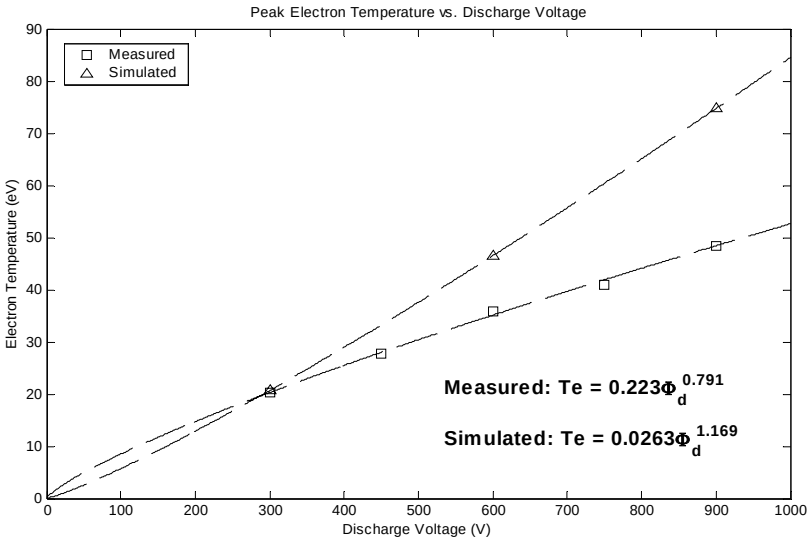

Figure 4.10 Plot of the peak electron temperature measured and simulated versus discharge voltage. Each set of data has been fit with a power law function.

The shape of the curves in Figure 4.10 have important significance for thruster designers and modelers. Because the electron temperature actually levels off as discharge voltage increases, erosion rates of the ceramic discharge walls will also level off with increasing discharge voltage. This leveling off arises because the strength of the voltage drop across the sheath is proportional to the electron temperature. As this sheath potential drop grows, ions strike the wall with more energy and cause increased sputtering upon impact. However, if the sheath drop growth is slowed with discharge voltage, the increase in erosion rate will slow as well. The electron temperature is also closely related to the plume divergence angle. The tangent of the divergence half angle is generally regarded as being proportional to the square root of electron temperature divided by discharge voltage,

$$\tan\theta_{1/2} \propto \sqrt{\frac{T_e}{\Phi_d}}, \tag{4.4}$$

because electron temperature typically controls radial expansion while discharge voltage determines the axial acceleration of the plume. It is interesting to note that if electron temperature behaves as suggested by the power law fit, the plume divergence angle will decrease with increasing discharge voltage. This phenomenon exists because the electron temperature is less than proportional to the discharge voltage.

One mechanism that might explain the discrepancy between the experimental and simulation data trends is secondary electron emission from the ceramic discharge chamber walls. As high energy electrons impact the boron nitride exit rings, low energy electrons are ejected into the plasma. If there is more secondary electron emission in reality than is modeled in the simulation, the bulk electron temperature would be reduced. As discharge voltage increases, electron temperature and energy increases as does the amount of secondary electron emission. It is possible that the PIC simulation does not account for all the secondary emission actually taking place within the thruster.

4.4 Azimuthal Variation of Plasma Properties

As previously mentioned, the interior five probes were spaced apart azimuthally to provide greater separation between the probes. This separation was done to ensure that there was no interaction between the probes that would affect the measurements. Although there were no specific tests performed to determine the azimuthal variation of plasma properties, the high and low voltage test setups utilized different azimuthal positions for probes 1-5 (see Table 3.2 and Table 3.3). Though the axial positions were also slightly different, a comparison of results can still be made. This comparison can be utilized to make some initial evaluations of the effect of azimuthal position on the probes. It can also be used to investigate the repeatability of test conditions between thruster firings.

The axial profiles of plasma properties should only be compared at the first five probe locations because the radial positions of the exterior probes were drastically different and therefore did not sample similar plasma regions. Comparisons were made for discharge voltages of 300V and 400V. Since there was no 400V data taken in the high voltage testing, a Lagrangian interpolation was used to produce 400V data from data taken at 300V, 450V and 600V. The axial profiles of electron temperature shown in Figure 4.11 match well at 300V in probes 1-5. The peak temperatures are very close in magnitude and the trends of rising electron temperature inside the channel are very similar. The 400V data do not match quite as well, but if the 400V data from the high voltage test were to have a peak between probes 4 and 5, it might be closer to the peak measured in the low voltage test. The trends are similar, but the high voltage data seems to begin the temperature rise further upstream.

The axial profiles of plasma potential and floating potential are compared in Figure 4.12 and Figure 4.13, respectively. In the regions of probes 1-4, the magnitudes of the potentials and the trends match very well, indicating that the plasma is similar over azimuthal angles. Some discrepancies arise at probe 5, and obviously large discrepancies occur in the outer probes due to their highly disparate locations between tests. It is important to

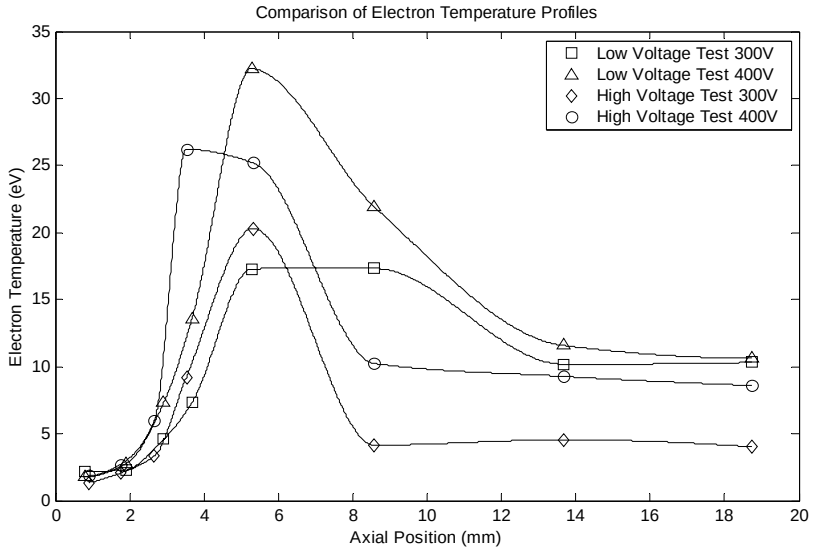

Figure 4.11 Comparison of axial profiles of electron temperature taken during the two different Langmuir probe tests.

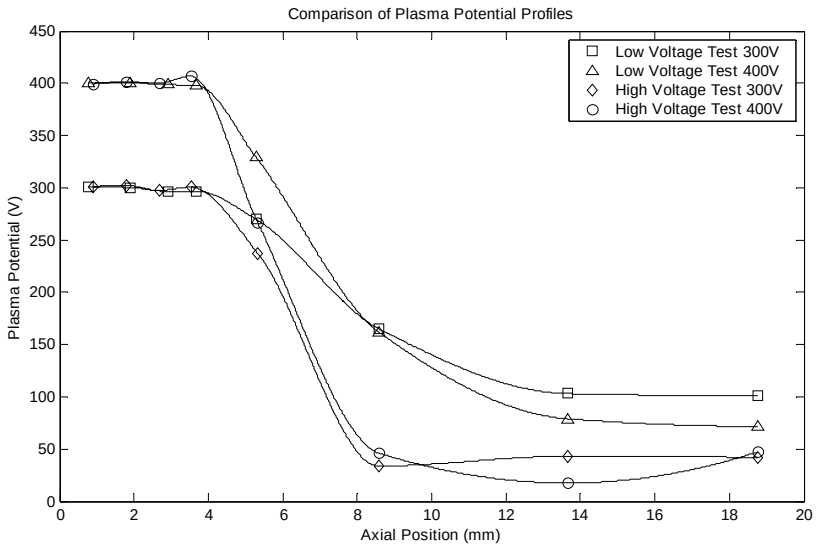

Figure 4.12 Comparison of axial profiles of plasma potential taken during the two different Langmuir probe tests.

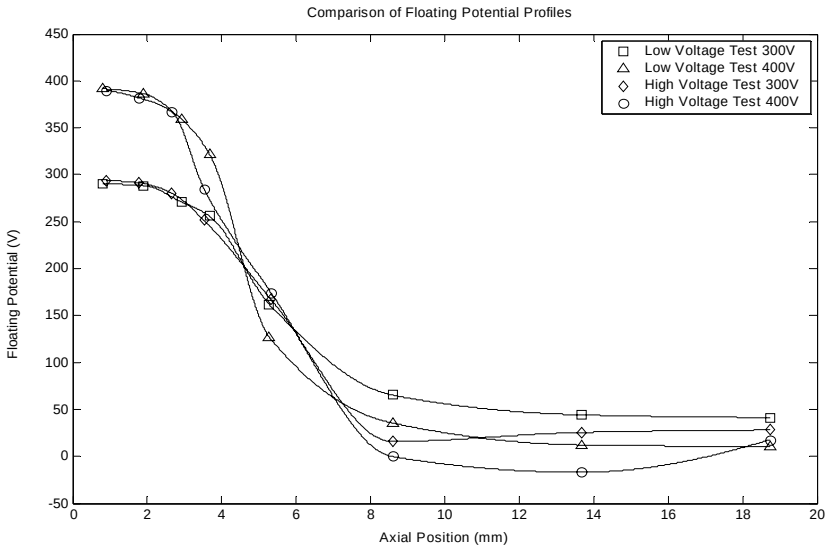

Figure 4.13 Comparison of axial profiles of floating potential taken during the two different Langmuir probe tests.

keep in mind that these separate tests were performed using different testing procedures and exit rings. The low voltage test was ordered in ascending discharge voltage (approximately), while the high voltage test was ordered in descending discharge voltage. Furthermore, the high voltage test used a newly manufactured exit ring with a sharp chamfer cut, while the low voltage test was performed with an older exit ring, which had a chamfer with rounded corners due to erosion.

The axial profiles of electron density are compared in Figure 4.14. Obvious differences in measured density were observed between the two different tests, as well as markedly different trends along the axial direction. One possible explanation for these differences is that the order of testing in the low voltage case may have meant that deposited layers were still being eroded from the exit ring surface during probe measurements, changing the test conditions. The data taken in the high voltage test were taken after many hours of thruster operation at high voltages where the high density discharge likely cleaned the exit ring surface before the data were recorded. Another possible explanation would be differences in azimuthal placement of the probes, although the former reason seems more likely since

some of the other plasma properties measured (particularly in the 300V data) indicate that there were no significant differences. It is clear that though azimuthal variation of the plasma properties seems unlikely, it cannot be ruled out.

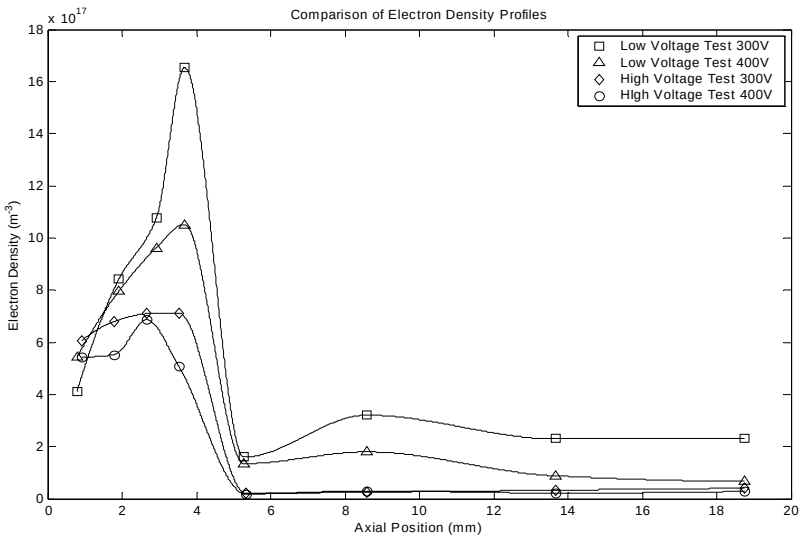

Figure 4.14 Comparison of axial profiles of electron density taken during the two different Langmuir probe tests.

Chapter 5

CONCLUSION

5.1 Conclusions

Performance testing and internal probe measurements were performed to support the ongoing development of computational models. The BHT-1000 was performance tested in both the single and two stage anode configurations. Specific impulse was shown to exceed 3000s at a discharge voltage of 1000V, while thrust efficiency was better than 50 percent. Two stage operation was shown to give some advantages in specific impulse and efficiency, although the amount of two stage testing was limited.

Internal probe measurements were made to determine axial profiles of plasma properties. These profiles were then compared to recent results of two dimensional particle-in-cell simulation of the BHT-1000. Experimental data compared well with results of the simulation, particularly in electron temperature and plasma potential results at lower voltages. Peak electron temperature was shown to depend on discharge voltage through a power law relationship for both the measured data and simulated plasma properties. However, the relationship between electron temperature and discharge voltage differed slightly between the experimental and simulated data. The peak electron temperature measured was less than proportional to discharge voltage, while the simulated value was actually more than proportional. The plots of electron density showed that there are still improvements to be made in the model, and that the simulation may in fact be "smearing" the plasma over too wide of an axial range. Despite some discrepancies in data between the experiment and

simulation, the probe measurements proved to be valuable data for code validation and benchmarking of the current status of theoretical models.

5.2 Recommendations

A few recommendations for further work in this area of research can be made. First, a thorough repetition of this work would be beneficial to fully determine the variability of results between test firings of the thruster. Qualitative observations made during this research have shown that it is difficult to repeat test conditions with very good accuracy. Second, an independent confirmation of results through a different type of experiment would add confidence to the findings presented here. This validation could be achieved through the use of emissive probes to determine plasma potential, or possibly optical methods to determine electron temperature and density. Third, this type of internal discharge probing could be used to determine plasma properties in the thruster while operating in the two stage configuration. The comparison of single and two stage profiles of plasma properties would be helpful in evaluating the effectiveness of two stage operation in separating the ionization and acceleration mechanisms. Finally, a study that correlated the plasma properties with thruster performance would be a helpful analysis for future thruster designers.

REFERENCES

[1] Hass, J. and Gallimore, A., "An Investigation of Internal Ion Number Density and Electron Temperature Profiles in a Laboratory-Model Hall Thruster," AIAA-00-3422, 36th Joint Propulsion Conference, Huntsville, AL, July 17-19, 2000.

[2] Staack, D., Raitses, Y., and Fisch, N. J., "Investigations of Probe Induced Perturbations in a Hall Thruster," AIAA-02-4109, 28th Joint Propulsion Conference, Indianapolis, IN, July 7-10, 2002.

[3] Raitses, Y., Ashkenazy, J. and Appelbaum, G., "Probe Measurements of Plasma Properties Inside and Experimental Hall Thruster," AIAA-98-3640, 34th Joint Propulsion Conference, Cleveland, OH, July 13-15, 1998.

[4] Kim, V., et al, "Local Plasma Parameter Measurements by Nearwall Probes Inside the SPT Accelerating Channel Under Thruster Operation with Kr," AIAA-02-4108, 38th Joint Propulsion Conference, Indianapolis, IN, July 7-10, 2002.

[5] Guerrini, G., et al, "Characterization of Plasma Inside the SPT-50 Channel by Electrostatic Probes," IEPC-97-053, 25th International Electric Propulsion Conference, Cleveland, OH, August 24-28, 1997.

[6] Szabo, J., "Fully Kinetic Numerical Modeling of a Plasma Thruster," Massachusetts Institute of Technology, Ph.D. Thesis, 2001.

[7] Sullivan, K., Martinez-Sanchez, M., Batishchev, O. and Szabo, J., "Progress on Particle Simulation of Ceramic-Wall Hall Thrusters," IEPC-03-278, 28th International Electric Propulsion Conference, Toulouse, France, March 17-21, 2003.

[8] Pote, B. and Tedrake, R., "Performance of a High Specific Impulse Hall Thruster," IEPC-01-35, 27th International Electric Propulsion Conference, Pasadena, CA, October 15-19, 2001.

[9] Pacros, A., "Instruments Design and Testing for a Hall Thruster Plume Experiment on the Space Shuttle," Massachusetts Institute of Technology, S.M. Thesis, 2002.

[10] Azziz, Y., "Instrument Development and Plasma Measurements on a 200-Watt Hall Thruster Plume," Massachusetts Institute of Technology, S.M. Thesis, 2003.

[11] Haag, T., "Design of a Thrust Stand for High Power Electric Propulsion Devices," AIAA-89-2829, 25th Joint Propulsion Conference, Monterey, CA, July 10-12, 1989.

[12] Haag, T. and Osborn, M., "RHETT/EPDM Performance Characterization," IEPC-97-107, 25th International Electric Propulsion Conference, Cleveland, OH, August 24-28, 1997.

[13] Manzella, D., et al, "High Voltage SPT Performance," AIAA-01-3774, 37th AIAA Joint Propulsion Conference, Salt Lake City, UT, July 8-11, 2001.

[14] Chung, P. M., Talbot, L. and Touryan, K. J., *Electrostatic Probes in Stationary and Flowing Plasmas*, Springer-Verlag, New York, 1975.

[15] Hutchinson, I. H., *Principles of Plasma Diagnostics*, Cambridge University Press, New York, 1987.

[16] Huddlestone, R. H. and Leonard, S. L., *Plasma Diagnostic Techniques*, Academic Press, New York, 1965.

[17] Lochte-Holtgreven, W., *Plasma Diagnostics*, North-Holland Publishing Company, Amsterdam, 1968.

[18] Fife, J. M., "Hybrid-PIC Modeling and Electrostatic Probe Survey of Hall Thrusters," Massachusetts Institute of Technology, Ph.D. Thesis, 1998.

[19] Hofer, R. R. and Gallimore, A. D., "Recent Results from Internal and Very-Near-Field Plasma Diagnostics of a High Specific Impulse Hall Thruster," IEPC-03-037, 28th International Electric Propulsion Conference, Toulouse, France, March 17-21, 2003.

[20] Warner, N., Szabo, J. and Martinez-Sanchez, M., "Characterization of a High Specific Impulse Hall Thruster Using Electrostatic Probes," IEPC-03-082, 28th International Electric Propulsion Conference, Toulouse, France, March 17-21, 2003.

[21] Jankovsky, R. S., et al, "NASA's Hall Thruster Program 2002," AIAA-02-3675, 38th Joint Propulsion Conference, Indianapolis, IN, July 7-10, 2002.

[22] Szabo, J., Martinez-Sanchez, M. and Batishchev, O., "Fully Kinetic Hall Thruster Modeling," IEPC-01-341, 27th International Electric Propulsion Conference, Pasadena, CA, October 15-19, 2001.

[23] Kim, V., et al, "Investigation of the Accelerated Ions Energy Accommodation Under Their Impingement with Solid Surfaces," AIAA-02-4110, 38th Joint Propulsion Conference, Indianapolis, IN, July 7-10, 2002.

[24] Szabo, J., Rostler, P., McElhinney, S. and Warner, N., "One and Two Dimensional Modeling of the BHT-1000," IEPC-03-231, 28th International Electric Propulsion Conference, Toulouse, France, March 17-21, 2003.

[25] Hass, J. and Gallimore, A., "Characterization of the Internal Plasma Structure of a 5 kW Hall Thruster," IEPC-99-078, 26th International Electric Propulsion Conference, Kitakyushu, Japan, October 17-21, 1999.

[26] Ahedo, E., Escobar, D., Perez, C. and Rus, J., "Parametric Investigation of the Hall Thruster Discharge," AIAA-03-4707, 39th Joint Propulsion Conference, Huntsville, AL, July 20-23, 2003.